Dear Editor, dear Reviewers,

Thank you very much for the time you have dedicated to review and comment our manuscript. We believe that your comments have helped us to improve significantly the quality of the work. Responses to the Referee's comment are organized according with the following index:

Referee's comment
Author's response
Changes in the manuscript

Kind regards, Yury Alkhimenkov, on behalf of the authors

Reply to Referee 1

Referee’s comment 1
I found the paper to be a good scientific contribution. I have recorded my comments in the attached pdf file. Please also note the supplement to this comment: https://www.solid-earth-discuss.net/se-2019-176/se-2019-176-RC1-supplement.pdf

Author’s reply 1
Dear Reviewer,

Thank you very much for the time you have dedicated to review and comment our manuscript. We believe that your comments have helped us to improve significantly the quality of the work. Please find below the responses to your comments.

Kind regards, Yury Alkhimenkov, on behalf of the authors

Changes in the manuscript 1
-

Referee’s comment 2

In this work, the authors use numerical methods to study the azimuth, angle and frequency-dependent seismic velocities for cracked rocks due to squirt flow. The authors do a rigorous 3D numerical study using simple geometry and set up two different experiments – connected and disconnected cracks. The authors show that the seismic velocities are dependent on azimuth, angle and frequency only for connected cracks case. The authors also compare the results of the disconnected crack with the high frequency results of the connected cracks case. Apart from Thomsen’s parameter that is primarily used for anisotropic studies in geophysics, the authors also formulate and use scalar parameter called anisotropy index parameter to describe the anisotropy dependence for squirt flow. This is a nice piece of numerical study for a simple geometry that gives new insights into anisotropy that arises due to squirt flow. The study is missing benchmarking of the numerical results with some simple analytical solutions or to some laboratory data. Benchmarking will help the readers have more confidence on the numerical results.

Author’s reply 2

We compared the results of our numerical solver against an analytical solution for squirt flow in a recently published manuscript [Alkhimenkov et. al., 2020]. Thus, we confirm that our numerical results are correct and accurate. There is no analytical solution for the presented model geometry, only the low and high-frequency limits can be described analytically. We extended the discussion section to include a qualitative comparison to the analytical solution.

Changes in the manuscript 2

Page 17, lines 352-365 (new subsection):

“A qualitative comparison against analytical models

Numerical simulations are useful but analytical models are especially attractive since they help us to better understand the physics and do not require sophisticated numerical simulations. The limitations of the analytical solutions are restricted to simple pore space geometry and some assumptions related to physics are needed to derive the closed form analytical formulas. Such a comparison of the numerical results against an analytical solution has been performed by Alkhimenkov et al. (2020) for a different pore space geometry. Unfortunately, there is no analytical solution for the present study considering a periodic distribution of intersecting cracks in three-dimensions. But the qualitative comparison of the low and high-frequency limits (which correspond to relaxed and unrelaxed states) is possible (Mavko and Jizba, 1991). Several analytical studies show that that the anisotropy (described by Thompson’s parameters) is, in general, more pronounced at high frequencies than at low frequencies (Guéguen, and Sarout, 2009, 2011). In the relaxed state, one can calculate the effective dry elastic moduli and use Gassmann's equations to obtain the effective moduli of the saturated medium. In the unrelaxed state, one can calculate the effective elastic moduli by restricting fluid flow (by using zero displacement boundary conditions in the cracks intersections). The low and high-frequency limits for elastic moduli have been calculated using these semi-analytical approaches and numerical results have been reproduced."

Referee's comment 3

I believe that the authors could make some comments on the practical uses of this in some details apart from the introduction section of the paper where they mention a generic statement on it.

Author's reply 3

We have extended the introduction of the manuscript and included more details on the practical uses.

Changes in the manuscript 3

Page 1, lines 15-23: "Wave propagation is controlled by the effective rock properties. Wave velocity and attenuation can be estimated from seismic data in scenarios such as exploration seismic, seismology, borehole measurements and tomography. Rock physics could then be used to estimate different rock properties, such as mineral composition, elastic moduli, the presence of a fluid, pore space connectivity (and, hence, permeability) from seismic measurements. Thus, investigation of how cracks and fluids affect seismic properties has many practical applications. In activities including nuclear waste disposal, CO2 geological sequestration, hydrocarbon exploration and production, geothermal energy production and seismotectonics, a quantification of the fluid content, porosity and permeability of rocks are of great interest. All these activities can benefit from rock physics studies, that is why cracked rocks have been under intensive studies during the last decades.

Referee's comment 4

Also, I think that the value of the work can be increased by application of the work on a real digital rock sample apart from the geometry that has been considered.

Author's reply 4

That's a very important point. A similar numerical workflow is used by my colleague Simon Lissa at the University of Lausanne to calculate the effective viscoelastic properties of 3D real digital rock samples. This project is ongoing.

Changes in the manuscript 4

-

Referee's comment 5

The authors can also think about presenting the figures for the results section in a better/simpler way (if possible). These figures are the crux of the paper and will be the most important thing for the readers to gain as a take-home message.

Author's reply 5

We agree that figures can be always improved, but at the same time, we don't want to simplify Figure 4 (for example) at the cost of showing less information. We insist on showing all components of the stiffness matrix in Figure 4, and later on simpler corresponding figures for P- and S-wave velocities are shown, as well as for the anisotropy measurements.

Changes in the manuscript 5

-

Referee's comment 6

I have mentioned my specific comments on the paper in the following section. General comments: Was any software (eg. COMSOL) used for the simulations?

Author's reply 6

Yes, we used a COMSOL Multiphysics PDE module where we implemented the equations in the weak form. Our results can be reproduced by using any open access finite element software. For that one needs a mesh generator (many open-access modules) and a solver of linear equations (many open access solvers).

Changes in the manuscript 6

Page 4, lines 98-100: "The COMSOL Multiphysics partial differential equation module is used for implementing equations (1) and (4) (displacement-stress formulation) in a weak form. Our numerical results can be fully reproduced by using any open-access software which include mesh generation and finite-element implementation with a corresponding solver of a linear system of equations.

Referee's comment 7

Can there be a way to apply this work for a real 3D digital rock sample?

Author's reply 7

Yes, the implementation is straightforward. One needs to use a digital rock image for the geometry and, the most difficult, the cracks must be resolved. After segmentation, our numerical workflow can be used. My colleague Simon Lissa at the University of Lausanne is working on this right now.

Changes in the manuscript 7

-

Referee's comment 8

Can the results be benchmarked with some standard analytical solution or measurements from the laboratory?

Author's reply 8

We compared the results of our numerical solver against an analytical solution for squirt flow in a recently published manuscript [Alkhimenkov et. al., 2020]. Thus, we confirm that our numerical results are correct and accurate. There is no analytical solution for the presented model geometry. Only the low and high-frequency limits can be described analytically and it has been verified in our study. We extended the discussion section to include a qualitative comparison to the analytical solution.

Changes in the manuscript 8

Page 17 (new subsection), see also Changes in the manuscript 2

Referee's comment 9

Specific comments: Comments on Introduction section: 1 st line is a good motivation for the study but leaves the reader with the question why or how cracked rocks play a crucial role. Some references or a line to elaborate it would be effective. One might argue that the next one mentions hydraulic properties are affected by cracks is the justification, however, I still think it deserves some clarity.

Author's reply 9

We extended the introduction.

Changes in the manuscript 9

Page 1, lines 15-23: “Wave propagation is controlled by the effective rock properties. Wave velocity and attenuation can be estimated from seismic data in scenarios such as exploration seismic, seismology, borehole measurements and tomography. Rock physics could then be used to estimate different rock properties, such as mineral composition, elastic moduli, the presence of a fluid, pore space connectivity (and, hence, permeability) from seismic measurements. Thus, investigation of how cracks and fluids affect seismic properties has many practical applications. In activities including nuclear waste disposal, CO2 geological sequestration, hydrocarbon exploration and production, geothermal energy production and seismotectonics, a quantification of the fluid content, porosity and permeability of rocks are of great interest. All these activities can benefit from rock physics studies, that is why cracked rocks have been under intensive studies during the last decades.”

Referee’s comment 10

Line 24 – Mesoscopic scale definition preferred before this line.Missing reference to Mavko and Nur (1975) classic paper that introduced “squirt flow”!

Author’s reply 10

We rearranged the paragraph and put the mesoscopic scale definition in the correct order. We also added the reference.

Changes in the manuscript 10

page 2, line 44: “This phenomenon, known as squirt flow (Mavko and Nur, 1975) causes strong energy dissipation due to the viscosity of the fluid and the associated viscous friction.”

Referee’s comment 11

Line 51 – Das et al. (2019) Numerical simulation of coupled fluid-solid interaction at the pore scale: A digital rock-physics technology is the full paper in Geophysics and is a better reference than the conference abstract.

Author’s reply 11

We changed the reference.

Changes in the manuscript 11

Page 2, line 57: “Das et al. (2019) numerically simulated a fully coupled fluid-solid interaction at the pore scale for digital rock samples.”

Referee’s comment 12

Comments on Numerical methodology section: Line 79 – Definition of u?

Author’s reply 12

We added the definition.

Changes in the manuscript 12

Page 3, line 84: “u is the displacement vector”

Referee’s comment 13

In the finite element numerical solver are you solving for displacement or velocity for the fluid phase (equation 3)? How is the coupling done in terms of displacement at the boundary between the two phases? It might be useful to mention a few lines here instead of just references.

Author's reply 13

We are solving the equations using displacement-stress formulation in the solid and fluid subdomains. The same displacement unknowns describe the solid and fluid displacement in the different regions. The equations (2) and (3) are combined and written in such a way that no specific boundary condition between the two phases must be specified.

Changes in the manuscript 13

Page 4, line 89-95: "In the finite element numerical solver, equations 2-3 are combined in the space-frequency domain $\sigma_{ij} = \lambda e\delta_{ij} + 2\mu\epsilon_{ij} + \boldsymbol{i}\omega\left(2\eta\epsilon_{ij} - \frac{2}{3}\eta e\delta_{ij}\right)$, where ϵ_{ij} are the components of the strain tensor $\epsilon_{ij} = 0.5\left(u_{i,j} + u_{j,i}\right)$, e is the trace of the strain tensor, λ and μ are the Lame parameters, u_i is the displacement in the i-th direction, δ_{ij} is the Kronekecker delta, $\boldsymbol{i}$ is the imaginary unit and ω is the angular frequency. In the domain representing a solid material, the equation 4 reduces to equation 2 by setting the shear viscosity η to zero. In the domain representing compressible viscous fluid, equation 3 is recovered by setting the shear modulus μ to zero."

Page 4, line 100: "The COMSOL Multiphysics partial differential equation module is used for implementing equations (1) and (4) (displacement-stress formulation) in a weak form."

Referee's comment 14

Line 86 – Why are the inertial terms neglected? What would be the limitations that might arise due to this approximation? Any discussion on how this can be included?

Author's reply 14

Inertial terms are neglected. When a propagating wave has a wavelength much larger than the inhomogeneities inside the medium, then the inhomogeneous medium properties can be replaced by its averaged properties, which correspond to the quasistatic experiment. The main limitation is the ratio between the wavelength λ and the length of our model domain L, so our results are valid when L divided by λ <<1. When this condition is not satisfied, then inertial terms are important and some wave scattering will be present. The inertial terms can be included but it will not affect our study since we are in the regime where inertial effects are negligible. The present author is working on a different study in the framework of poroelasticity considering inertial effects, so these results will be available in the future.

Changes in the manuscript 14

-

Referee's comment 15

Line 88 – Why is the PARDISO solver used? The reader might wander what are the advantages of using this versus any other solver.

Author's reply 15

We tested several available solvers and found that PARDISO solver gives the best performance for our numerical model configuration and computing system. MUMPS (MUltifrontal Massively Parallel Sparse direct Solver) converges to the same result as PARDISO but it uses 30$\%$ more RAM memory and two times slower. Iterative solvers could not converge. That is most likely due to a very heavy numerical model. We believe that PARDISO solver is good only for our specific applications, therefore we do not discuss this choice. For other model geometry, another solver might give better results. For example, a colleague of mine who is working on 3D digital rock images found that MUMPS direct solver is more robust than PARDISO solver.

Changes in the manuscript 15

-

Referee's comment 16

Line 89 – What is direct relaxation test? Reference/ one line description can be useful.

Author's reply 16

A direct relaxation test is a numerical test when we apply specific displacement boundary conditions in such a way that one specific component of the stiffness matrix can be calculated. So the word "direct" has the meaning that one specific cij component is calculated at the end. (A more detailed explanation of boundary conditions is presented in the appendix A.) This "direct approach" is in contrast to approaches that perform, for example, 4 relaxation tests to calculate 5 stiffness components, one or two "indirectly".

Changes in the manuscript 16

Page 4, lines 103-107: "The basic idea of the direct relaxation tests is that a displacement boundary condition of the form $u = 10^{-6} \times \exp(i\omega t)$ is applied to a certain external wall of the model and in a certain direction, while at other walls of the model, the displacements are set to zero or let free to change. In the direct tests that we perform, only one component of the stiffness matrix cij can be directly calculated after one numerical simulation. A detailed description of the boundary conditions is given in Alkhimenkov et al. (2020)."

Referee's comment 17

Line 96 – Is the harmonic displacement a function of time? Are you solving the equations in time domain or frequency domain? How does combining equations 2 and 3 work if the equations are solved in time domain vs frequency domain?

Author's reply 17

In our numerical simulations, the harmonic displacement is a function of frequency and we solve equations in the space-frequency domain. In other words, time derivatives are replaced by $i\omega$. The coupling is the same in the time domain and in the frequency domain, the only difference is $i\omega$. We performed our study in the frequency domain, therefore, we do not discuss how to solve the corresponding equations in the time domain.

Changes in the manuscript 17

Page 4, lines 88-96: "In the finite element numerical solver, equations (2)-(3) are combined in the space-frequency domain (see equation 4)."

Also, see Changes in the manuscript 16

Referee's comment 18

Line 100 – What are mixed direct tests?

Author's reply 18

This is explained in Appendix A. A mixed direct test is similar to the direct relaxation test. Diagonal components of the stiffness matrix cij can be calculated directly, i.e. by using direct tests. A mixed test for non-diagonal components (c12, c13, c23) is necessary plus the result of the direct test of the corresponding diagonal element to calculate the non-diagonal elements (c12, c13, c23). In Appendix A we presented the corresponding equations as well as boundary conditions for direct and mixed direct tests. Also, see Changes in the manuscript 16.

Changes in the manuscript 18

-

Referee's comment 19

Comments on Numerical model: Line 108 Any specific reason for having an aspect ratio of 0.01?

Author's reply 19

There is always a compromise between the crack aspect ratio and the possibility to perform the numerical simulation. In our simulations, we need several elements inside the crack to resolve fluid flow and the parabolic fluid velocity profile. Therefore, if the aspect ratio is very low (meaning that for a given crack length one decreases crack thickness), one will need too many elements, so at some point, it becomes impossible to solve the problem due to RAM memory limitations. Therefore, we found a compromise. With such an aspect ratio of 0.01, we have enough elements inside the crack and the total number of elements is not too big (around 3 million), so we can solve the problem.

Changes in the manuscript 19

-

Referee's comment 20

Line 109 Any specific reason for using glycerol?

Author's reply 20

Yes. In the laboratory, glycerol is usually used in order to shift the characteristic frequency to lower frequencies and, thus, to measure dispersion and attenuation. We used glycerol also for this purpose, and consequently to qualitatively compare our characteristic frequency to that of a forced oscillation laboratory experiment.

Changes in the manuscript 20

-

Referee's comment 21

Line 110 In Table 1, how is the Bulk Modulus (K) of the fluids used in equation 3?

Author's reply 21

There is a fluid pressure p in equation 3. The pressure is the volumetric part of the stress tensor with a "minus" sign. The volumetric part of the stress tensor is related to the strain tensor via the fluid bulk modulus K.

Changes in the manuscript 21

See Changes in the manuscript 13

Referee's comment 22

Line 111 Can there be some quantitative ways of describing fine and coarser mesh – size of the elements (maximum and minimum size, average size of the mesh element) including the details mentioned in the caption of Figure 2. Also, along the z axis of the mesh, parts of it has 3 elements as per the snapshot in Figure 2. Is this sufficient number of elements from numerical point of view? Is there any way to justify that the numerical solution is stable with the number of elements used?

Author's reply 22

We have the mesh sizes (minimum and maximum) in the caption to figure 2. The numerical tests suggest that 3 elements along the z-axis is a sufficient number of elements to converge to the correct result, we performed several tests similar to those of Quintal et. al, (2019). The stability can be justified in a naive way, by increasing the number of elements and comparing solutions, which we also tested.

Changes in the manuscript 22

-

Referee's comment 23

Line 113 What type of system configuration was used for making the simulations? It seems like 0.95TB of RAM would require very specific type of machine to run. How much time did it take to run each of the simulation?

Author's reply 23

We used an intel node: dual socket E5-2683 v4 @ 2.1GHz (32 cores), 1024 GB RAM. For each frequency, it takes about 2.5 hours. There are 12 calculations for each component, 9 components of the stiffness matrix were calculated. So, for each model, it took 2.5x12x9=270 hours to calculate the full stiffness matrix. Since we have two models (with connected and disconnected cracks), the total number is 540 computer hours giving 22.5 days. In total more calculations were performed because we checked convergence and performed other tests, so in the end, the total number of machine-hours is even larger.

Changes in the manuscript 23

Page 5, lines 129-132:

"The simulation is performed for 12 different frequencies from 10^1 to $10^{6.5}$ Hz for each of the nine components of the stiffness matrix (c11, c22, c33, c12, c13, c23, c44, c55, c66). For each frequency, the solver uses approximately 0.95 Terabyte of RAM memory and takes approximately 2.5 hours on 32 Intel dual-socket E5-2683 v4 2.1 GHz (1024 GB RAM) cores."

Referee's comment 24

Line 126-127 Does the difference between the stiffness of the two disconnected cracks also depend on the boundary conditions applied to the system? In other words, will the stiffness be always different irrespective of the boundary condition applied?

Author's reply 24

Our results for the effective properties are independent of our boundary conditions. However, several studies show that, for example, stress and strain boundary conditions might give different results and this has to be carefully considered (Milani et al., 2016, Geophysics). With respect to the difference between connected and disconnected cracks, there will be always a difference present for any type of boundary condition.

Changes in the manuscript 24

-

Referee's comment 25

Comments on Results section:Line 147 Unclear what is meant by the cracks can be described by only two compliances as per equation 6?

Author's reply 25

The effect of a crack embedded into the linear elastic material can be quantified by the means of the so-called stiffness contribution tensor or alternatively by the two parameters — normal and tangential crack compliances Zn and Zt. For that, we need an effective compliance matrix of the background material and crack compliance Zn and Zt. It can be seen from equation 7: once we invert the matrix cij and get the compliance matrix sij, Zn and Zt can be inverted (Zn can be inverted from s22 or s33 and Zt can be inverted from s44).

Changes in the manuscript 25

-

Referee's comment 26

I am also confused that in Line 142 it is mentioned that there is a significant difference due to vertical crack separation. However, in Line 148, it is mentioned that only connected cracks case is considered? Can this be explained better?

Author's reply 26

We removed this sentence which is indeed confusing.

Changes in the manuscript 26

Page 8. Lines 164-170, we removed one sentence

Referee's comment 27

Line 165 – What are the values of frequencies used for LF, Fc and HF?

Author's reply 27

The values are 10^1 Hz for LF, 10^4 Hz for Fc and $10^{6.5}$ HZ for HF.

Changes in the manuscript 27

We modified the caption of figure 3.

"Snapshots of the fluid pressure Pf in the cracks at three different frequencies: LF - the low-frequency limit (corresponds to 10^1 Hz, relaxed state), Fc - intermediate frequency snapshot (corresponds to 10^4 Hz, close to the characteristic frequency) and HF - the high-frequency limit (corresponds to $10^{6.5}$ Hz, unrelaxed state)."

Referee's comment 28

Line 173 – It is unclear what is meant by the elastic limit in this case? Can this be compared to any standard elastic limits that are mentioned in literature?

Author's reply 28

In our numerical simulation, the grain material is elastic while fluid is not, fluid can diffuse which is described by viscosity. In the high-frequency limit, there is no time for fluid to flow, so it behaves as an elastic material having bulk properties of glycerol and zero shear modulus. We do not understand exactly what the referee meant by the standard elastic limit but the configuration simply corresponds to a fully elastic material where the fluid behaves as a solid with zero shear modulus.

Changes in the manuscript 28

-

Referee's comment 29

Figure 4 might be improved from a reader's perspective.

Author's reply 29

Simplified information derived from the data presented in Figure 4 is shown in the subsequent figures. We know that it shows a lot of curves, but we prefer showing everything in this figure for the sake of completeness.

Changes in the manuscript 29

-

Referee's comment 30

Line 180 – Even in figure 4a, the Real part of the c22 and c33 component coincides. Is there a specific reason for pointing out separately the attenuation and dispersion components are the same due to symmetry of the model?

Author's reply 30

The dispersion and attenuation of c22 and c33 components are the same due to the symmetry of the model and the same geometrical characteristics of the cracks. For example, the model can be symmetric but the two cracks might have different stiffness due to different fluid or asperities of the crack walls, etc.

Changes in the manuscript 30

-

Referee's comment 31

Line 183 – It might be useful to explain what negative attenuation means in physical sense. Is there a reason for the negative attenuation behavior?

Author's reply 31

Now, this is explained in the text.

Changes in the manuscript 31

Page 4, lines 118-120:

"Note that usually the inverse quality factor is used as a measure of attenuation (O'connell and Budiansky, 1978). In this study, we show the inverse quality factor for each component of the stiffness tensor, even though the ratio Im(cij(omega))=Re(cij(omega)) does not represent attenuation of any corresponding wave mode for some components."

Page 9, Lines 199-209: "The c12 and c13 components are non-dispersive, the c23 component exhibits strong negative dispersion and a negative inverse quality factor peak shifted towards high frequencies compared to that of the c22, c33 components. A similar phenomenon has been reported by Guo et al. (2017) in the context of two-dimensional simulations. The c23 component does not correspond to a wave mode alone, it is always used together with c22 or/and c33 components. Therefore, no wave will gain energy. This negative inverse quality factor sign for the c23 component was also verified using Kramers-Kronig relations. In other words, different components of the stiffness tensor might have positive or negative values of the ratio Im(c23)=Re(c23) but when we calculate the velocity and the inverse quality factor of a wave, the cumulative effect of all cij components must be physical and no negative attenuation will be observed."

Referee's comment 32

Line 194 – It might be useful to mention how the seismic velocities are calculated as a function of phase?

Author's reply 32

Now, this is better explained in the text.

Changes in the manuscript 32

Page 10, lines 118-220: "The P- and S-wave phase velocities are calculated by solving the Christoffel equation which represents an eigenvalue problem relating the stiffness components cij , the phase velocities of plane waves that propagate in the medium and the polarization of the waves (Fedorov, 1968; 220 Tsvankin, 2012)."

Referee's comment 33

Figure 6 – Is there a reason for the discrepancy between V_{SV} between the disconnected crack model and the high-frequency result at a phase angle of 0, 90 and 180 degrees?

Author's reply 33

Yes, indeed, there is a slight discrepancy between the connected and disconnected crack models in terms of V_{SV} velocities at specific angles. In fact, such discrepancy is very small, less than 0.6 $\%$. The nature of this discrepancy is due to the crack separation. If the model is dry, the discrepancy is huge, as explained in the paper. For the fluid-saturated model, the discrepancy is small but it still exists and can be visible at V_{SV} velocities.

Changes in the manuscript 33

Page 11, lines 236-238: "A slight discrepancy (around 0.5%) between the SV-wave velocities for the disconnected crack model (Figure 6, dashed red line) and the high-frequency velocity for the connected crack model (Figure 6, green line) at phase angles of 0, 90 and 180 degrees is due to the crack separation."

Referee's comment 34

Comments related to Discussions: Line 311 – What are the model parameters that the conclusion will depend upon? The authors mention about the need of sensitivity analysis of the model parameters. It would be useful to give a qualitative idea about the possible model parameters that the results will depend on.

Author's reply 34

That is an important point and the most difficult to answer. Basically, all model parameters affect the effective response. In order to give a precise answer one must run the sensitivity study for all parameters. Since for one set of parameters we needed around 22 days of continuous calculations, for a decent sensitivity study, it would require years with our current computational power. In our opinion, the most important parameters are the crack density, crack compliance, crack orientation and the saturation of the cracks.

Changes in the manuscript 34

Page 18, lines 380-387: "In summary, squirt flow does affect effective mechanical properties of cracked rocks and, thus, seismic velocity anisotropy. Given that seismic anisotropy variations with frequency are very sensitive to the pore space geometry and material properties, it is difficult to make a general prediction. According to our study, the effective frequency-dependent response of a cracked medium is different in different planes. The local response (in a certain plane) is controlled by cracks orientation, which is the key parameter. The magnitude of the frequency-dependent response (i.e. the dispersion and attenuation) is controlled by crack compliances, crack porosity and their fluid content (dry or liquid-saturation will cause completely different behavior). Most importantly, crack porosity is a very important parameter in fluid-saturated rocks (contrary to dry rocks) since it defines the volume of fluid content which may flow due to wave propagation, causing wave attenuation and dispersion."

References:

Alkhimenkov, Y., Caspari, E., Gurevich, B., Barbosa, N. D., Glubokovskikh, S., Hunziker, J., & Quintal, B. (2020). Frequency-dependent attenuation and dispersion caused by squirt flow: Three-dimensional numerical study. Geophysics, 85(3), 1-71.

Quintal, B., Caspari, E., Holliger, K., & Steeb, H. (2019). Numerically quantifying energy loss caused by squirt flow. Geophysical Prospecting, 67(8), 2196-2212.

Milani, M., Rubino, J. G., Müller, T. M., Quintal, B., Caspari, E., & Holliger, K. (2016). Representative elementary volumes for evaluating effective seismic properties of heterogeneous poroelastic mediaREVs for heterogeneous porous media. Geophysics, 81(2), D169-D181.

Reply to Referee 2

Referee's comment 1

The paper is focused on a numerical model aiming at calculating the frequency and anisotropic response of a saturated cracked rock for a passing seismic wave. The model provides a numerical calculation following the previous work of B. Quintal. The model considers two orthogonal thin cracks embedded in a homogenous background. Two situations are examined: the two cracks are either connected or disconnected. The numerical method has been previously used by Quintal (2016, 2019). It consists in applying relaxation tests to a viscoelastic medium. The CIJ constants are obtained by averaging.

Author's reply 1

Dear Reviewer,

Thank you very much for the time you have dedicated to review and comment our manuscript. We believe that your comments have helped us to improve significantly the quality of the work. Please find blow the responses to your comments.

Kind regards, Yury Alkhimenkov, on behalf of the authors

Changes in the manuscript 1

-

Referee's comment 2

Several remarks are the following. First the frequency dependent curves extend over a broad frequency range, for a unique crack aspect ratio. This implies that squirt flow would never be focused on a narrow frequency range (unless the system size plays a dominant role in the calculation). This remark is important for the geophysical im-plications: Fig. 4a shows that the width of the attenuation peak (at half amplitude) is about one order and half magnitude.

Author's reply 2

That's indeed true. Although several analytical solutions predict a narrow frequency range, for example, Gurevich et al., (2010) and Collet and Gurevich (2016), we published results showing a broad frequency range for squirt flow in a different paper [Alkhimenkov et. al., 2020] considering a different pore-space geometry. For the pore-space geometry presented in the current manuscript we again consistently observe that squirt flow is not focused on a narrow frequency range.

Changes in the manuscript 2

Page 10, line 207-209:

"Note that the width of the inverse quality factor peak (at half amplitude) for the components c22 and c33 is about one order and half magnitude (Figures 4a and 4c). It means that attenuation and dispersion due to squirt flow play a significant role over a broad frequency range even for cracks with a single aspect ratio."

Referee's comment 3

Second, the model considers two cracks of 0.1m in a cube of 0.24 m size. In terms of crack density, this means a very high crack density (close to 1). This is consistent with the large decrease of C22 and C33 in the dry case, compared to the original values of the intact rock (table 1). But such high values are not realistic.

Author's reply 3

Yes, indeed, the crack density is quite high. This is a synthetic study and all physical effects will be the same for a medium with a smaller crack density (the magnitude will be smaller). According to our calculations, our crack density is closer to 0.1. $p = 1/0.24^{3}0.1^{3} * 2 = 0.1447$, where 0.24m – a cuboid size, 0.1m - the radius of the crack, 2 - the number of the cracks. This is a correct formula for cracks with random orientations [Bristow, J. R., 1960; Kachanov, M., & Mishakin, V. V. 2019]. For our model geometry, this definition can be considered as a rough approximation. A better definition for our geometry requires the usage of the crack density tensor (second-order) plus another fourth order tensor [Kachanov, M., & Mishakin, V. V. 2019].

Changes in the manuscript 3

-

Referee's comment 4

Third, Fig. 4c shows a negative 1/Q and a very high dispersion for C23. Probably, the negative sign (which is unphysical) is an error of convention. But the high value (almost 0.4 for 1/Q) should be related to the very high crack density (i.e. the size of the system) and the low value of C23.

Author's reply 4

Yes, indeed the dispersion as well as "attenuation" for the C23 component is strong. First, the negative sign for "attenuation" is correct. We are not the first who observe this negative ratio of Im(C23)/Re(C23). For example, Guo et. al. (2017) already reported a negative sign in their results of 2D numerical simulations. Let us first discuss the negative sign and, then, why the value of 1/Q is high.

The C23 component is the coupling component between C22 and C33 components. In the stiffness tensor, we do have high and low limits for components which are based on the energy constraints. When we are talking about wave dispersion and attenuation in anisotropic media, we should consider all stiffness components which are needed to calculate wave speeds and attenuations. The C23 component does not enter any wave mode in any direction alone, the C23 component is always used together with C22 or/and C33, which have high positive values of attenuation. Therefore, no wave will gain energy. In other words, different components of the stiffness tensor might have positive or negative values of "attenuation" but when we calculate the velocity and attenuation of a wave, the cumulative effect of all Cij components must be physical (it can be seen in Figures 5-7) and no negative attenuation will be observed. This negative "attenuation" sign for C23 was also verified using Kramers-Kronig relations. We think that there is a terminology issue. In fact, we have a negative value of the ratio Im(C23)/Re(C23), but it might be misleading to call that attenuation, which is associated with the characteristic of a wave following a definition based on energy-related considerations.

The high negative value of Im(C23)/Re(C23) is due to the low values of C23 in figure 4c (17 GPa or 7 GPa). It is related to the high crack density in our model geometry but for a model with lower crack density, we think, that the negative value of Im(C23)/Re(C23) will be also high.

Now in the manuscript, we refrain from using the terminology "attenuation" for the ratio Im(C23)/Re(C23). We now simply refer to it as a ratio and we reserve the terminology attenuation for wave modes. Furthermore, the wave modes as explained above won't ever show a negative attenuation.

Changes in the manuscript 4

Page 4, line 118-120: "Note that usually the inverse quality factor is used as a measure of attenuation (O'connell and Budiansky, 1978). In this study, we show the inverse quality factor for each component of the stiffness tensor, even though the ratio Im(cij(omega))=Re(cij(omega)) does not represent attenuation of any corresponding wave mode for some components."

Page 9, lines 199-206: "The c12 and c13 components are non-dispersive, the c23 component exhibits strong negative dispersion and a negative inverse quality factor peak shifted towards high frequencies compared to that of the c22, c33 components. A similar phenomenon has been reported by Guo et al. (2017) in the context of two-dimensional simulations. The c23 component does not correspond to a wave mode alone, it is always used together with c22 or/and c33 components. Therefore, no wave will gain energy. This negative inverse quality factor sign for the c23 component was also verified using Kramers-Kronig relations. In other words, different components of the stiffness tensor might have positive or negative values of the ratio Im(c23)=Re(c23) but when we calculate the velocity and the inverse quality factor of a wave, the cumulative effect of all cij components must be physical and no negative attenuation will be observed."

Referee's comment 5

Four, although a precise comparison is impossible, it would be of interest to discuss these results against (effective medium) calculations published some years ago (Guéguen, Y. , and Sarout,J., 2009. Crack-induced anisotropy in crustal rocks: predicted dry and fluid-saturated Thomsen's parameters. Physics of the Earth and Planetary Interiors, 172, 116-124; and Guéguen, Y. , and Sarout, J., 2011. Characteristics of anisotropy and dispersion in cracked medium. Tectonophysics, 503, 1-2, 165-172.) In both cases, the goal is similar but the methods differ. In terms of anisotropic compliances dispersion, it seems (from a first check) that the predictions of GS agree with the present results. They give a prediction of dispersion for Sijkl in terms of the two crack density tensors alpha and beta. Non-zero values are predicted only if the i,j,k,l index is 2 or 3 (given the cracks orientations in the present case).

Author's reply 5

We compared the results of our numerical solver against an analytical solution for squirt flow in a recently published manuscript [Alkhimenkov et. al., 2020]. There is no analytical solution for the presented model geometry, only the low and high-frequency limits can be described analytically. Guéguen, and Sarout, (2009, 2011) presented analytical models considering poroelastic and squirt flow effects at low and high-frequency limits. They observe that the anisotropy (described by Thompson's parameters) is, in general, more pronounced at high frequencies than at low frequencies.

Changes in the manuscript 5

page 2, line 47-50: "There are several analytical solutions for squirt flow (O'Connell and Budiansky, 1977; Dvorkin et al., 1995; Chapman et al., 2002; Guéguen and Sarout, 2009, 2011; Gurevich et al., 2010) which are based on simplified pore geometries and many physical assumptions."

Page 17, line 352-365 (new subsection):

"A qualitative comparison against analytical models

Numerical simulations are useful but analytical models are especially attractive since they help us to better understand the physics and do not require sophisticated numerical simulations. The limitations of the analytical solutions are restricted to simple pore space geometry and some assumptions related to physics are needed to derive the closed form analytical formulas. Such a comparison of the numerical results against an analytical solution has been performed by Alkhimenkov et al. (2020) for a different pore space geometry. Unfortunately, there is no analytical solution for the present study considering a periodic distribution of intersecting cracks in three-dimensions. But the qualitative comparison of the low and high-frequency limits (which correspond to relaxed and unrelaxed states) is possible (Mavko and Jizba, 1991). Several analytical studies show that that the anisotropy (described by Thompson's parameters) is, in general, more pronounced at high frequencies than at low frequencies (Guéguen, and Sarout, 2009, 2011). In the relaxed state, one can calculate the effective dry elastic moduli and use Gassmann's equations to obtain the effective moduli of the saturated medium. In the unrelaxed state, one can calculate the effective elastic moduli by restricting fluid flow (by using zero displacement boundary conditions in the cracks intersections). The low and high-frequency limits for elastic moduli have been calculated using these semi-analytical approaches and numerical results have been reproduced."

Referee's comment 6

In conclusion, this is an interesting paper.

25 January 2020 Yves Guéguen.

Author's reply 6

Thank you for your comments, which helped us to improve significantly the manuscript.

Changes in the manuscript 6

-

References:

Alkhimenkov, Y., Caspari, E., Gurevich, B., Barbosa, N. D., Glubokovskikh, S., Hunziker, J., & Quintal, B. (2020). Frequency-dependent attenuation and dispersion caused by squirt flow: Three-dimensional numerical study. Geophysics, 85(3), 1-71.

Bristow, J. R. (1960). Microcracks, and the static and dynamic elastic constants of annealed heavily cold-worked metals. British Journal of Applied Physics, 11,81–85.

Kachanov, M., & Mishakin, V. V. (2019). On crack density, crack porosity, and the possibility to interrelate them. International Journal of Engineering Science, 142, 185-189.

Guo, J., Rubino, J. G., Glubokovskikh, S., & Gurevich, B. (2017). Effects of fracture intersections on seismic dispersion: theoretical predictions versus numerical simulations. Geophysical Prospecting, 65(5), 1264-1276.

Azimuth-, angle- and frequency-dependent seismic velocities of cracked rocks due to squirt flow

Yury Alkhimenkov[1][2], Eva Caspari[3], Simon Lissa[1], and Beatriz Quintal[1][2]

[1]Institute of Earth Sciences, University of Lausanne, Lausanne, Switzerland
[2]Swiss Geocomputing Centre, University of Lausanne, Lausanne, Switzerland
[3]Chair of Applied Geophysics, Montanuniversity Leoben, Leoben, Austria

Correspondence: Yury Alkhimenkov (yury.alkhimenkov@unil.ch)

Abstract. Understanding the properties of cracked rocks is of great importance in scenarios involving CO_2 geological sequestration, nuclear waste disposal, geothermal energy ~~,~~ and hydrocarbon exploration and production. Developing non-invasive detecting and monitoring methods for such geological formations is crucial. Many studies show that seismic waves exhibit strong dispersion and attenuation across a broad frequency range due to fluid flow at the pore scale known as squirt flow. Nevertheless, how and to what extent squirt flow affects seismic waves is still a matter of investigation. To fully understand its angle- and frequency-dependent behavior for specific geometries appropriate numerical simulations are needed. We perform a three-dimensional numerical study of the fluid-solid deformation at the pore scale based on coupled Lamé-Navier and Navier-Stokes linear quasistatic equations. We show that seismic wave velocities exhibit strong azimuth-, angle- and frequency-dependent behavior due to squirt flow between interconnected cracks. We show that the overall anisotropy of a medium mainly increases due to squirt flow but in some specific planes the anisotropy can locally decrease. We analyze the Thomsen-type anisotropic parameters and adopt another scalar parameter which can be used to measure the anisotropy strength of a model with any elastic symmetry. This work significantly clarifies the impact of squirt flow on seismic wave anisotropy in three dimensions and can potentially be used to improve the geophysical monitoring and surveying of fluid-filled cracked porous zones in the subsurface.

1 Introduction

~~Cracked rocks have been under intensive studies during the last decades since they play a crucial role in CO_2 geological sequestration,~~

Wave propagation is controlled by the effective rock properties. Wave velocity and attenuation can be estimated from seismic data in scenarios such as exploration seismic, seismology, borehole measurements and tomography. Rock physics could then be used to estimate different rock properties, such as mineral composition, elastic moduli, the presence of a fluid, pore space connectivity (and, hence, permeability) from seismic measurements. Thus, investigation of how cracks and fluids affect seismic properties has many practical applications. In activities including nuclear waste disposal, ~~geothermal energy and~~ CO_2 geological sequestration, hydrocarbon exploration and production~~.~~, geothermal energy production and seismotectonics, a quantification of the fluid content, porosity and permeability of rocks are of great interest. All these activities can benefit from rock physics studies, that is why cracked rocks have been under intensive studies during the last decades.

Cracks and grain-scale discontinuities are the key rock parameters which control effective elastic and hydraulic properties of such rocks. Many studies show that seismic waves exhibit significant dispersion and attenuation in cracked porous rocks due to pore-scale fluid flow (O'Connell and Budiansky, 1977; Dvorkin et al., 1995; Gurevich et al., 2010; Müller et al., 2010). Furthermore, cracks cause significant seismic wave anisotropy (Schoenberg and Sayers, 1995; Sayers and Kachanov, 1995; Sayers, 2002; Chapman, 2003; Maultzsch et al., 2003; Tsvankin and Grechka, 2011). ~~Thus, seismic methods can be used to detect and characterize cracked zones and may be useful to predict crack density, their preferred orientation and interconnectivity of cracks.~~

~~One candefine fractures as discontinuities at the mesoscopic scale and cracks as discontinuities at the pore scale.~~ Fluid flow due to a passing wave may happen at different scales: at the wavelength scale, at the mesoscopic scale and at the pore scale (Müller et al., 2010). Biot's theory (Biot, 1962) describes the so-called global flow at the wavelength scale but its overall effect on a passing wave at seismic frequencies is usually much smaller than that of fluid flow at the mesoscopic and pore scales (Pride et al., 2004). Mesoscopic scale is that much larger than the pore-scale but smaller than the wavelength. At this scale, studies are performed in the framework of Biot theory, assuming heterogeneous rock properties. One can define fractures as discontinuities at the mesoscopic scale and cracks as discontinuities at the pore scale. There are several analytical and numerical studies on the effect of wave-induced fluid flow between mesoscopic fractures and a porous rock background and between interconnected fractures using the Biot's equations (Brajanovski et al., 2005; Rubino et al., 2013; Quintal et al., 2014; Masson and Pride, 2014; Grab et al., 2017; Hunziker et al., 2018; Caspari et al., 2019) as well as on the comparison between the numerical and analytical results ~~(Guo et al., 2017a, 2018)~~(Guo et al., 2017b, 2018). Experimental studies of synthetic rock samples showed the impact of fluid-saturated fractures on seismic velocities (Amalokwu et al., 2016; Tillotson et al., 2012, 2014). The resulting frequency-dependent anisotropy was analysed by Carcione et al. (2013); Rubino et al. (2017); Barbosa et al. (2017). The last two also considered fracture-to-fracture flow, in addition to fracture-to-background flow.

At the pore scale, a passing wave induces fluid pressure gradients which occur between interconnected cracks, as well as, between cracks and stiffer pores. Such pressure gradients force fluid to move between different cracks and pores until the pore pressure equilibrates throughout the connected pore space. This phenomenon, known as squirt flow (Mavko and Nur, 1975) causes strong energy dissipation due to the viscosity of the fluid and the associated viscous friction. Several experimental studies confirmed the importance of squirt flow at different frequency ranges (Mayr and Burkhardt, 2006; Best et al., 2007; Adelinet et al., 2010; Mikhaltsevitch et al., 2015; Pimienta et al., 2015; Subramaniyan et al., 2015; Chapman et al., 2019). There are several analytical solutions for squirt flow ~~(O'Connell and Budiansky, 1977; Dvorkin et al., 1995; Chapman et al., 2002; Gurevich et al., 2010~~ (O'Connell and Budiansky, 1977; Dvorkin et al., 1995; Chapman et al., 2002; Guéguen and Sarout, 2009, 2011; Gurevich et al., 2010) which are based on simplified pore geometries and many physical assumptions.

Dispersion and attenuation caused by squirt flow can be simulated numerically by solving the coupled fluid-solid deformation at the pore scale using Lame-Navier and Navier-Stokes equations with appropriate boundary conditions and, then, calculating effective frequency-dependent viscoelastic properties. During the last decades, many studies used numerical methods to solve mechanical problems (Andrä et al., 2013a, b; Saxena and Mavko, 2016). Recently, some numerical studies appeared in the geophysical literature aiming to solve the coupled fluid-solid deformation and, hence, studying dispersion and attenuation caused by squirt flow ~~(Zhang et al., 2010; Zhang and Toksöz, 2012; Quintal et al., 2016, 2019; ?; ?). ?~~ (Zhang et al., 2010; Zhang and Toksöz, 201 . Das et al. (2019) numerically simulated a fully coupled fluid-solid interaction at the pore scale for digital rock samples. They modeled the pore fluids as Newtonian fluids using the Navier-Stokes equation with appropriate coupling between both the solid and liquid phases, accounting for inertial effects. Quintal et al. (2016, 2019) simplified the Navier-Stokes equations by ~~assuming compressible Stokes flow,~~ neglecting inertial term and, hence, using the linearized quasistatic Navier-Stokes equation.

We numerically simulate squirt flow in three dimensions and calculate frequency-dependent effective stiffness moduli using the finite-element method to solve the quasi-static Lamé-Navier equations coupled to the linearized quasi-static Navier-Stokes equations ~~(Quintal et al., 2016, 2019; ?)~~(Quintal et al., 2016, 2019; Alkhimenkov et al., 2020). We apply an oscillatory deformation to certain boundaries of the numerical model, and, assuming that the wavelength is much larger than the size of individual cracks, we calculate the volume average stress and strain fields and the resulting effective stiffness moduli. Then, we calculate the associated azimuth-, angle- and frequency-dependent seismic velocities by solving the Christoffel equation. The main goal of this study is to analyse seismic anisotropy due to squirt flow in three dimensions since the previous numerical studies of seismic anisotropy were performed only in two dimensions and in the framework of Biot's theory (Rubino et al., 2017; Barbosa et al., 2017).

This paper is organized as follows. First, we briefly describe the numerical methodology. Then, we describe the numerical model and show the numerical results — frequency-dependent effective stiffness moduli. After, by solving the Christoffel equation, we evaluate the angle-, azimuth- and frequency dependent velocities of the model. Lastly, we quantify the anisotropy strength of the models analyzing the conventional Thomson-type anisotropy parameters and also by adopting another scalar parameter.

2 Numerical methodology

We consider that at the pore scale, a rock is composed by a solid material (grains) and a fluid-saturated pore space (cracks). The numerical methodology is described by Quintal et al. (2016, 2019) and ~~?~~ Alkhimenkov et al. (2020) and here we briefly outline the main equations. The solid phase is described as a linear isotropic elastic material for which the conservation of momentum is (e.g., Landau and Lifshitz (1959b) and Nemat-Nasser and Hori (2013))

$$\nabla \cdot \boldsymbol{\sigma} = 0, \tag{1}$$

where "$\nabla \cdot$" denotes the divergence operator acting on the stress tensor $\boldsymbol{\sigma}$. The infinitesimal stress-strain relation for an elastic material can be written as

$$\boldsymbol{\sigma} = (K - \frac{2}{3}\mu)\mathbf{tr}\left(\frac{1}{2}\left((\nabla \otimes \mathbf{u}) + (\nabla \otimes \mathbf{u})^{\mathrm{T}}\right)\right)\mathbf{I}_2 + 2\mu\left(\frac{1}{2}\left((\nabla \otimes \mathbf{u}) + (\nabla \otimes \mathbf{u})^{\mathrm{T}}\right)\right) \tag{2}$$

where $\mathbf{I}_2$ is the second order identity tensor, $\mathbf{tr}$ is the trace operator, "$\otimes$" defines the tensor product, the superscript "$^{\mathrm{T}}$" corresponds to the transpose operator, $\mathbf{u}$ is the displacement vector, K and μ are the bulk and shear moduli.

The fluid phase is described by the quasi-static linearised compressible Navier-Stokes momentum equation (Landau and Lifshitz, 1959a):

$$-\nabla p + \eta\nabla^2 v + \frac{1}{3}\eta\nabla\left(\nabla\cdot v\right) = 0, \tag{3}$$

where v is the particle velocity, p is the fluid pressure and η is the shear viscosity. Equation (3) is valid for the laminar flow of a Newtonian fluid. In the finite element numerical solver, equations (2)-(3) are combined in the space-frequency domain

$$\sigma_{ij} = \lambda e\delta_{ij} + 2\mu\epsilon_{ij} + \boldsymbol{i}\omega\left(2\eta\epsilon_{ij} - \frac{2}{3}\eta e\delta_{ij}\right), \tag{4}$$

where ϵ_{ij} are the components of the strain tensor $\epsilon_{ij} = 0.5\left(u_{i,j} + u_{j,i}\right)$, e is the trace of the strain tensor, λ and μ are the Lame parameters, u_i is the displacement in the i-th direction, δ_{ij} is the Kronekecker delta, $\boldsymbol{i}$ is the imaginary unit and ω is the angular frequency. In the domain representing a solid material, the equation (4) reduces to equation (2) by setting the shear viscosity η to zero. In the domain representing compressible viscous fluid, equation (3) is recovered by setting the shear modulus μ to zero. The solid and fluid displacements are described by the same variable and, thus, naturally coupled at the boundaries between subdomains (Quintal et al., 2016, 2019). In ~~this simulation~~the simulations, the energy dissipation is caused only by fluid pressure diffusion, since inertial terms are neglected.

The COMSOL Multiphysics partial differential equation module is used for implementing equations (1) and (4) (displacement-stress formulation) in a weak form. Our numerical results can be fully reproduced by using any open access software which include mesh generation and finite-element implementation with a corresponding solver of a linear system of equations. The whole spatial domain is discretized using an unstructured mesh with tetrahedral elements. A direct PARDISO solver (Schenk and Gärtner, 2004) is used for solving the linear system of equations. Direct relaxation tests are performed to compute all components of the stiffness matrix (in Voigt notation) c_{ij}. ~~The boundary conditions are applied to the external~~ The basic idea of the direct relaxation tests is that a displacement boundary condition of the form $u = 10^{-6}\times\exp(\boldsymbol{i}\omega t)$ is applied to a certain external wall of the model and in a certain direction, while at other walls of the model~~.~~, the displacements are set to zero or let free to change. In the direct tests that we perform, only one component of the stiffness matrix c_{ij} can be directly calculated after one numrical simulation. A detailed description of the boundary conditions is given in Alkhimenkov et al. (2020). The initial conditions for displacements are set to zero. The resulting stress and strains are averaged over the spatial domain for each frequency. Then, the complex valued $c_{ii}(\omega)$ components (diagonal) are calculated for each frequency (in Voigt notation, no index summation):

$$c_{ii}(\omega) = \frac{\langle\sigma_i(\omega)\rangle}{\langle\epsilon_i(\omega)\rangle}, \tag{5}$$

where $\langle\cdot\rangle$ represents the volume averaging over the sample volume.

For calculating the P-wave modulus ($ii = 11, 22, 33$), a harmonic displacement on the i direction is applied perpendicularlly to a wall of the model. At the other walls of the model, the normal component of the displacement is set to zero. For calculating shear components of the stiffness matrix ($ii = 44, 55, 66$), the boundary conditions applied are those of a simple shear test. ~~A detailed description of the boundary conditions is given in ?.~~ For the $c_{12}(\omega)$, $c_{13}(\omega)$ and $c_{23}(\omega)$ components (off-diagonal), mixed direct tests are needed, and the corresponding boundary conditions are given in Appendix A. The corresponding inverse quality factor is (O'connell and Budiansky, 1978)

$$\frac{1}{Q_{ij}(\omega)} = \frac{\mathrm{Im}\left\{c_{ij}(\omega)\right\}}{\mathrm{Re}\left\{c_{ij}(\omega)\right\}} \frac{\mathrm{Im}\left(c_{ij}(\omega)\right)}{\mathrm{Re}\left(c_{ij}(\omega)\right)}. \tag{6}$$

Note that usually the inverse quality factor is used as a measure of attenuation (O'connell and Budiansky, 1978). In this study, we show the inverse quality factor for each component of the stiffness tensor, even though the ratio $\mathrm{Im}\left(c_{ij}(\omega)\right)/\mathrm{Re}\left(c_{ij}(\omega)\right)$ does not represent attenuation of any corresponding wave mode for some components.

3 Numerical model

Two 3D numerical models are constructed, which consist of a pore space embedded into an elastic solid grain material (Figure 1). The solid grain material is represented by a cuboid whose size is $(0.24 \times 0.24 \times 0.24)$ m^3. The pore space consists of two perpendicular cracks represented by thin cylinders of 0.002 m thickness, 0.1 m radius (i.e., the aspect ratio is thickness divided by diameter — 0.01) and fully saturated with a liquid. In the first model, the two cracks are disconnected, while, in the second model, the two cracks are connected (cross sections in Figure 1). The employed liquid properties are those of glycerol and the grain material has properties of quartz (Table 1).

A fine, regular mesh is used inside the crack to accurately account for dissipation, while in the grain material the mesh is coarser (Figure 2). The total number of elements is 3.3×10^6. The simulation is performed for ~~13~~ 12 different frequencies from 10^1 to ~~10^7 Hz~~ $10^{6.5}$ Hz for each of the nine components of the stiffness matrix (c_{11}, c_{22}, c_{33}, c_{12}, c_{13}, c_{23}, c_{44}, c_{55}, c_{66}). For each frequency, the solver uses approximately 0.95 Terabyte of RAM memory ~~.~~ and takes approximately 2.5 hours on 32 Intel dual-socket E5-2683 v4 2.1 GHz (1024 GB RAM) cores.

One crack embedded into an isotropic background induces a transverse isotropy (5 independent components of the stiffness tensor e.g., Mavko et al. (2009)). If the crack is parallel to the xy-plane, then the symmetry is vertical and the medium exhibits vertical transverse isotropy — VTI symmetry. If the crack is parallel to the xz-plane, then the symmetry is horizontal and the medium exhibits horizontal transverse isotropy — HTI symmetry. If two cracks, perpendicular to each other are embedded into an isotropic material and the crack compliances are different, then the medium exhibits orthorhombic symmetry (9 independent components of the stiffness tensor). If the the crack compliances are the same, then the medium symmetry is tetragonal (6 independent components of the stiffness tensor); some authors attribute this geometry to a special case of orthorhombic symmetry (e.g., Bakulin et al. (2000b)), while tetragonal and orthorhombic symmetry classes are different. On the other hand, one can argue that an orthorhombic medium (created by two perpendicular sets of cracks) degenerates into a tetragonal medium if the cracks compliances are the same.

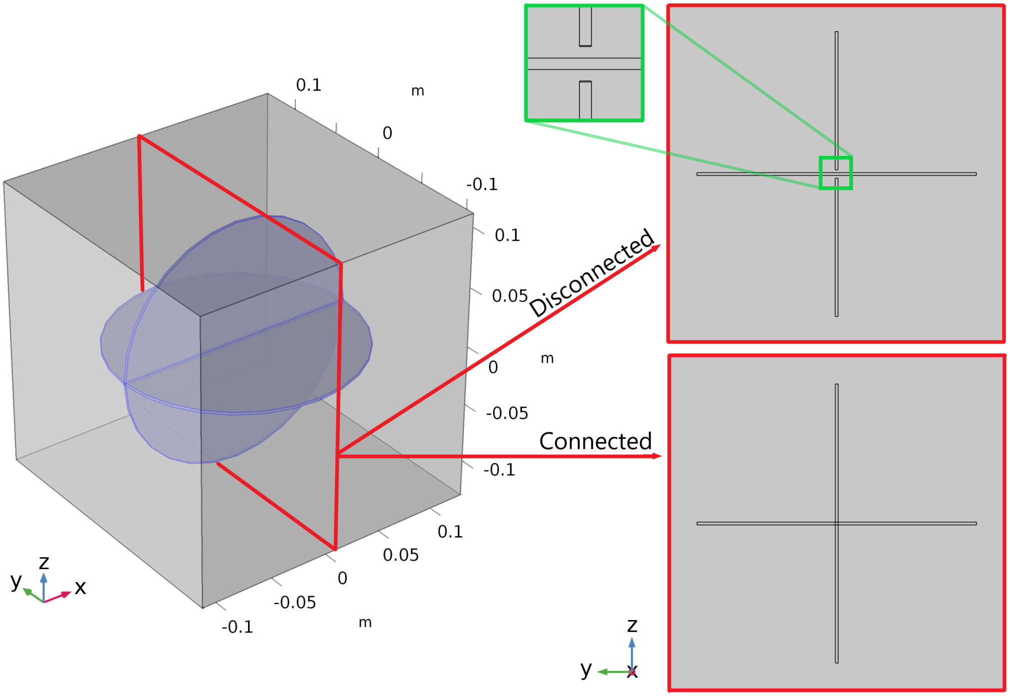

Figure 1. Sketch illustrating two flat cylinders representing two cracks. The blue region represents the pore space saturated with a fluid, the transparent gray area corresponds to the solid grain material. In the first model, the two cracks are disconnected as illustrated by the upper right cartoon. In the second model, the two cracks are connected as illustrated by the down right cartoon.

The symmetry of the saturated numerical model with connected cracks is tetragonal (Figure 1) because the crack compliances are the same. Thus, there are only six independent components of the stiffness tensor. We will see that the symmetry of the saturated numerical model with disconnected cracks is orthorhombic because one crack is stiffer than the other one due to its separation into two parts. ~~But~~ However, the difference between c_{22} and c_{33} stiffness components is less then 0.3%, thus the divergence from the tetragonal symmetry is negligible and, therefore, this model is considered as tetragonal as well.

Table 1. Material properties of the numerical model

Material property	quartz	glycerol	air
Bulk modulus K	36 GPa	4.3 GPa	1.01×10^{-4} GPa
Shear modulus μ	44 GPa	—	—
Shear viscosity η	—	1.414 Pa·s	1.695×10^{-5} Pa·s

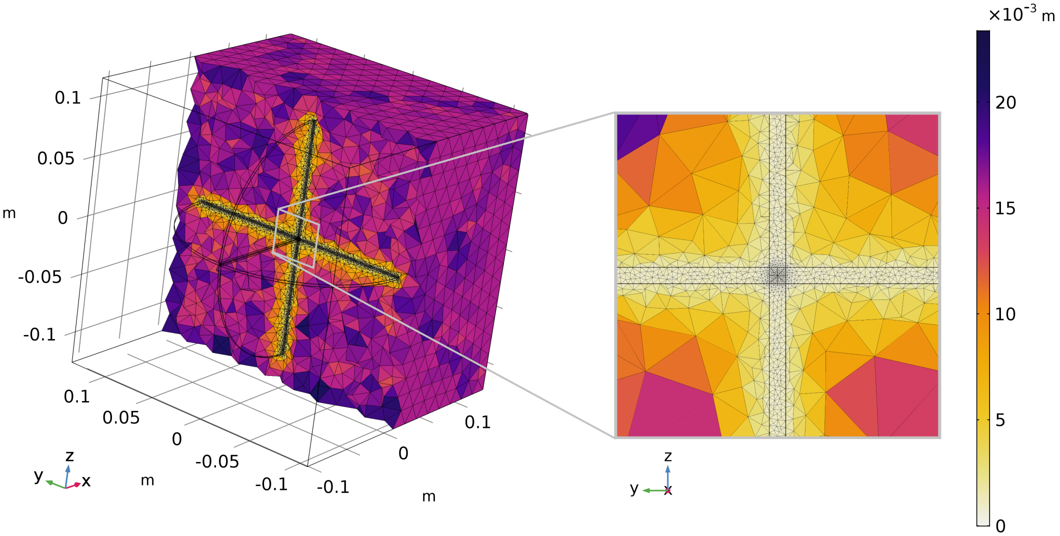

Figure 2. Sketch illustrating the element's size distribution for the model with connected cracks. Element's size in the crack is $5 \times 10^{-5} - 1 \times 10^{-3}$ m and in the surrounding grain material is $2.4 \times 10^{-3} - 1.6 \times 10^{-2}$ m. The element's size distribution for the model with disconnected cracks is the same.

4 Results

4.1 Dry stiffness moduli

Let's first consider the geometry shown in Figure 1 with a pore space filled with air (i.e. dry). We perform nine relaxation tests to calculate the full stiffness tensor for each of the two models with connected and disconnected cracks. The resulting effective stiffness moduli for the model with connected cracks are (in Voigt notation)

$$c_{ij}^{Con} = \begin{bmatrix} 93.53 & 4.65 & 4.65 & 0 & 0 & 0 \\ 4.65 & 63.91 & 5.46 & 0 & 0 & 0 \\ 4.65 & 5.46 & 63.91 & 0 & 0 & 0 \\ 0 & 0 & 0 & 31.62 & 0 & 0 \\ 0 & 0 & 0 & 0 & 35.16 & 0 \\ 0 & 0 & 0 & 0 & 0 & 35.16 \end{bmatrix} (\text{GPa}). \tag{7}$$

For the model with disconnected cracks, the effective stiffness moduli are (in Voigt notation)

$$c_{ij}^{Dis} = \begin{bmatrix} 93.55 & 4.92 & 4.60 & 0 & 0 & 0 \\ 4.92 & 69.21 & 4.40 & 0 & 0 & 0 \\ 4.60 & 4.40 & 64.06 & 0 & 0 & 0 \\ 0 & 0 & 0 & 31.95 & 0 & 0 \\ 0 & 0 & 0 & 0 & 35.16 & 0 \\ 0 & 0 & 0 & 0 & 0 & 36.96 \end{bmatrix} (\text{GPa}). \tag{8}$$

The effective stiffness moduli of the two models are different. Zero values are written if the value is below 0.0002 GPa (i.e. up to numerical precision). The c_{ij}^{Con} stiffness matrix precisely belongs to the tetragonal symmetry class while the c_{ij}^{Dis} stiffness matrix has all diagonal components different from each other, thus, it represents the orthorhombic symmetry class. The largest difference between c_{ij}^{Con} and c_{ij}^{Dis} is in the c_{22} component, i.e., $\Delta c_{22} = c_{ij}^{Dis} - c_{ij}^{Con} = 5.3$ GPa. That is a significant difference and it is only due to the vertical crack separation.

There are two different features which must be clearly separated: 1) The effect of cracks ~~intersections~~ intersection without changing the cracks geometry on the effective elastic properties. In this case, the crack intersection is achieved by changing the spatial position of the cracks. Grechka and Kachanov (2006) studied numerically the effect of cracks ~~intersections~~ intersection without changing the crack geometry. They concluded that ~~crack intersections~~ cracks intersection have a very little impact on the effective elastic moduli. ~~In this study, we formally consider only the model with connected cracks and we show that cracks can be accurately described by only two compliances which can be seen in equation .~~ 2) The effect of the crack partition into two "halves" on the effective elastic properties. In this case, the partitioned crack has a long thin contact area across the whole diameter (Figure 1). It is well known that the ~~islands of contacts~~ contact areas inside a crack significantly reduce crack compliance ~~(a crack with contact areas is stiffer compared to the same crack but without contacts~~ (Trofimov et al., 2017; Kachanov and Sevostianov, 2018; Markov et al., 2019; Lissa et al., 2019)~~)~~. Comparing eq. (7) and (8), ~~this study also shows that~~ we also observe that the thin contact area significantly ~~reduce~~ reduces the crack compliance: the effective dry moduli of the model with disconnected cracks are much ~~stiffer~~ higher compared to the model with connected cracks.

An intuitive explanation is the following: if ~~the cracks surface~~ cracks surfaces have not been changed by changing the spatial position of the cracks in the volume — the effect of ~~crack intersections~~ cracks intersection is negligible (Grechka and Kachanov, 2006); if the cracks ~~surface~~ surfaces have been changed, as we did in the present study by partitioning the vertical crack into two pieces (and introducing a thin additional contact area) — the effective elastic moduli would become much stiffer compared to the model where the cracks ~~surface~~ surfaces has not been changed.

4.2 Fluid pressure fields

Here and later on we deal only with a liquid-saturated pore space. The liquid has properties of glycerol (Table 1). A direct P-wave modulus test is performed to calculate dispersion and attenuation ~~of~~ for the c_{33} component (a harmonic displacement is applied to the top wall of the model in z-direction, while the normal component of the displacement is set to zero on all the other walls). Figure 3 shows snapshots of the fluid pressure P_f in the cracks at three different frequencies, in the vertical middle slice of the model (the yz plane, red frame in Figure 1 (left)). For the model with connected cracks, at low frequencies, there is enough time for pressure equilibration between the cracks, thus, the pore pressure is uniform throughout the pore space (Figure 3, LF (connected)). This is called the relaxed state. At intermediate frequencies, there is a large pressure gradient in the cracks, which corresponds to the maximum attenuation due to squirt flow between cracks (Figure 3, Fc (connected)). At high frequencies, there is no time for fluid to move, hence, there is no fluid pressure equilibration between the vertical and horizontal cracks (Figure 3, HF (connected)). This is called the unrelaxed state. Therefore, at high frequencies, the connected cracks behave as hydraulically isolated and the fluid highly stiffens the crack. In the model with disconnected cracks, the fluid pressure in the cracks is the same in all three regimes which corresponds to the unrelaxed state in the model with connected cracks. The unrelaxed state can be interpreted as the elastic limit because there is no fluid flow between the cracks and the effective properties of the two models (connected and disconnected cracks) are the same, as will be shown in the next subsection.

4.3 Dispersion and attenuation

4.3.1 Elastic moduli

Figure 4 shows the numerical results for the complex-valued frequency-dependent components of the stiffness matrix $c_{ij}(\omega)$ (in Voigt notation) for the models with connected and disconnected cracks filled with glycerol. In the model with connected cracks, the ~~dispersion (the~~ real part of the c_{ij} component ~~) and attenuation~~ and the corresponding inverse quality factor (eq. (6)) curves show strong frequency-dependent behavior of the c_{22}, c_{33} and c_{23} components (~~Figure 4, (a) and(c)). The attenuation~~ Figures 4a and 4c). The inverse quality factor and dispersion of the c_{22}, c_{33} components coincide because the geometrical properties of the two cracks are the same (Figure 4~~, (a)~~ a) and the model is symmetric. The c_{11} component is non-dispersive and exhibit zero attenuation. The dispersion of the c_{44}, c_{55} and c_{66} components is negligible and these components exhibit also negligible attenuation (Figure 4~~, (b)). The~~ b). The c_{12} and c_{13} components are non-dispersive, the c_{23} component exhibits strong negative dispersion and ~~the attenuation peak is~~ a negative inverse quality factor peak shifted towards high frequencies compared to that of the c_{22}, c_{33} components. ~~The c_{12} and c_{13} componentsare non-dispersive and exhibit zero attenuation .~~ A similar phenomenon has been reported by Guo et al. (2017b) in the context of two-dimensional simulations. The c_{23} component does not correspond to a wave mode alone, it is always used together with c_{22} or/and c_{33} components. Therefore, no wave will gain energy. This negative inverse quality factor sign for the c_{23} component was also verified using Kramers-Kronig relations. In other words, different components of the stiffness tensor might have positive or negative values of the ratio $\mathrm{Im}(c_{23})/\mathrm{Re}(c_{23})$ but when we calculate the velocity and the inverse quality factor of a wave, the cumulative effect of all c_{ij} components must be physical and no negative attenuation will be observed.

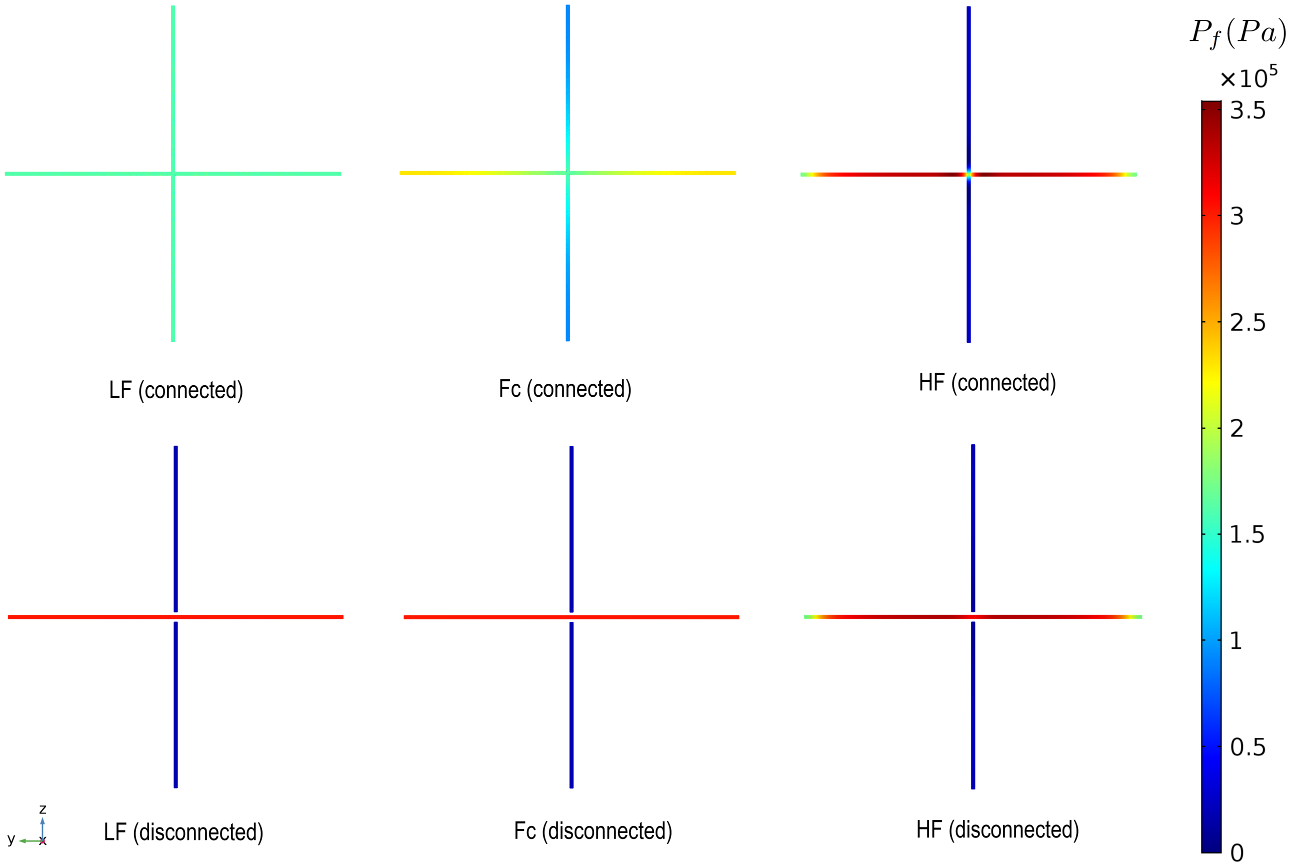

Figure 3. Snapshots of the fluid pressure P_f in the cracks at three different frequencies: ~~Lf~~ LF - the ~~low frequency~~ low-frequency limit (corresponds to 10^1 Hz, relaxed state), Fc - intermediate frequency snapshot (corresponds to 10^4 Hz, close to the characteristic frequency) and HF - the ~~high frequency~~ high-frequency limit (corresponds to $10^{6.5}$ Hz, unrelaxed state).

Note that the width of the inverse quality factor peak (at half amplitude) for the components c_{22} and c_{33} is about one order and half magnitude (Figures 4a and 4c). It means that attenuation and dispersion due to squirt flow play a significant role over a broad frequency range even for cracks with a single aspect ratio.

In the model with disconnected cracks, all components of the stiffness tensor $c_{ij}(\omega)$ (~~Figure 4, (a-c)~~Figures 4a and 4c) are constant across the whole frequency range and ~~exhibit zero attenuation~~exhibit zero inverse quality factor. Furthermore, all components are approximately equal to the ~~high frequency~~ high-frequency values of the model with connected cracks. This is expected in the unrelaxed state because the connected cracks behave as hydraulically isolated with respect to fluid flow. A very small discrepancy between the two models at high frequencies is associated with the vertical crack partition (two thin regions of pore space replaced with stiffer grain material).

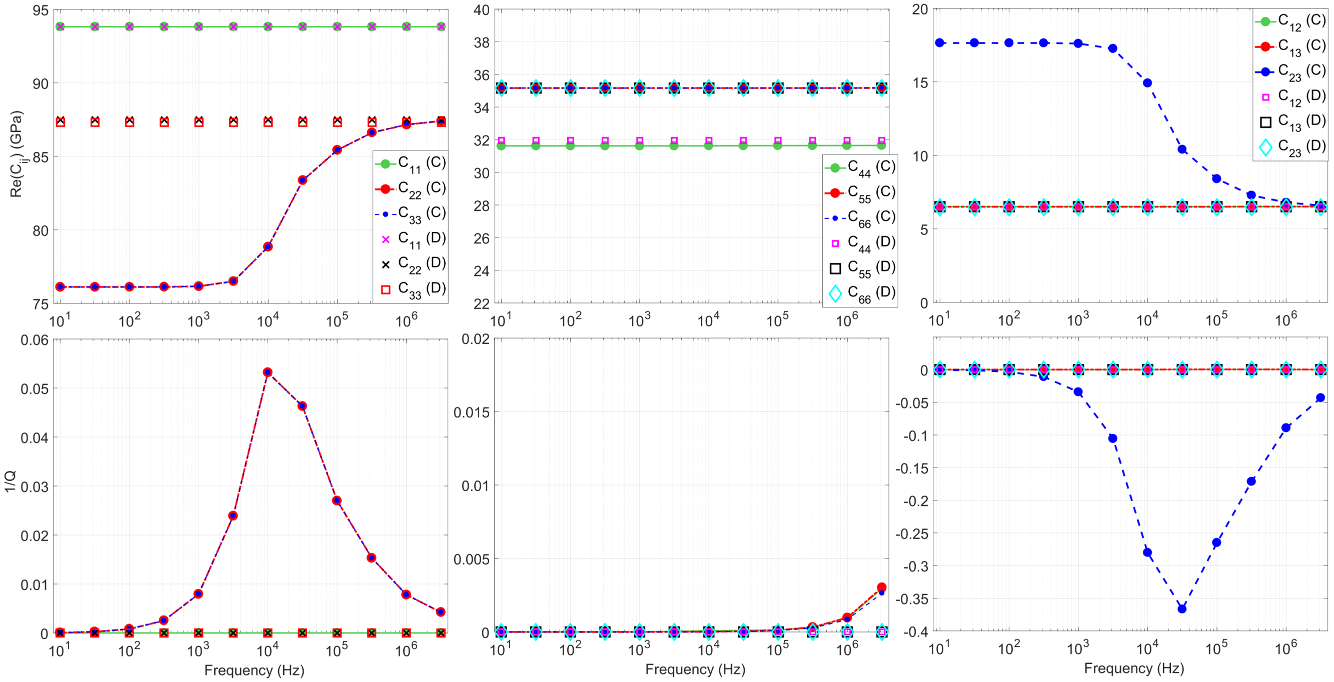

Figure 4. Numerical results for the connected (C) and disconnected (D) cracks models: ~~(a-c)~~ Real part of the c_{ij} components versus frequency (upper plots), dimensionless ~~attenuation~~ inverse quality factor of the c_{ij} components versus frequency (lower plots). Each symbol corresponds to the test result of one numerical simulation and lines correspond to linear interpolation between discrete numerical results.

4.3.2 ~~Seismic~~ P- and S-wave velocities

Figure 5 shows the P-wave (primary wave) phase velocity as a function of the phase angle of the numerical model with connected and disconnected cracks (Figure 1), where the zero phase angle corresponds to the vertical wave propagation (along z- axis). The P- and S-wave phase velocities are calculated by solving the Christoffel equation which represents an eigenvalue problem relating the stiffness components c_{ij}, the phase velocities of plane waves that propagate in the medium and the polarization of the waves (Fedorov, 1968; Tsvankin, 2012). Considering the plane YZ, the P-wave velocity is the same for phase angles of 0 and 90 degrees, it changes with frequency only for phase angles between 0 and 90 degrees and is maximal in the ~~high frequency~~ high-frequency limit at phase angle of $\theta = 90(\pm 90)$ degrees (Figure 5, left). Furthermore, in the ~~high frequency~~ high-frequency limit the P-wave phase velocity coincides for the models with connected and disconnected cracks. As frequency decreases, the P-wave velocity decreases and at 10^4 Hz the P-wave velocity is almost angle independent (yellow curve, Figure 5, left). It is interesting that this "local" isotropy corresponds to the maximum attenuation of the c_{22} and c_{33} components (Figure 4). As frequency further decreases, the P-wave velocity decreases and stays nearly unchanged for the frequencies below $10^{3.5}$ Hz. In the XZ-plane, the P-wave phase velocity is the same for the models with connected and

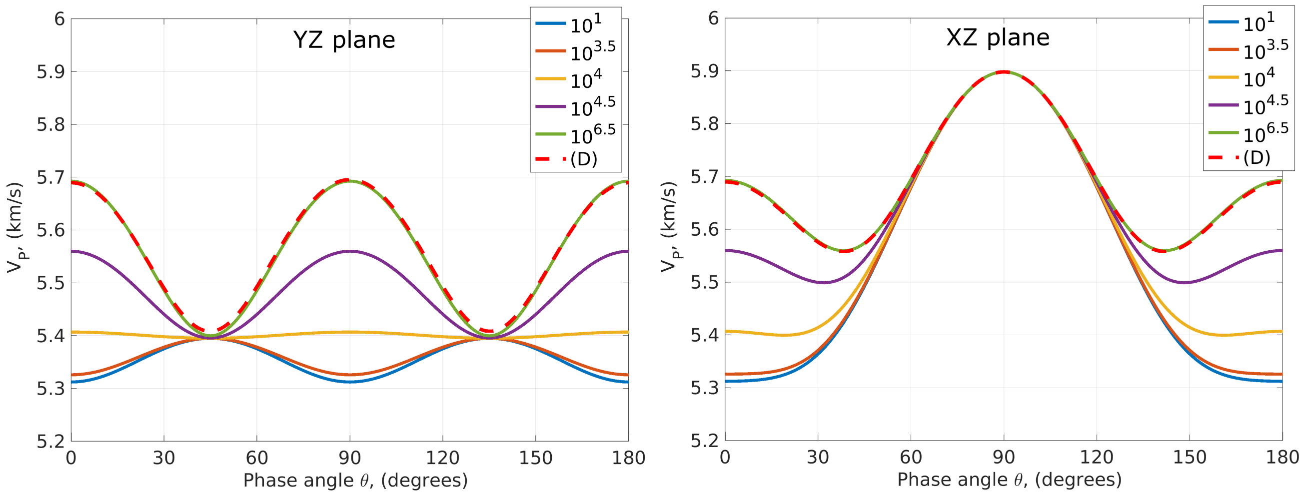

Figure 5. P-wave phase velocity versus phase angle in the YZ-plane (left) and the XZ-plane (right). Curves 10^1-$10^{6.5}$ denote the frequency of the P-wave for the model with connected cracks. (D) — denotes the P-wave for the model with disconnected cracks.

disconnected cracks in the ~~high frequency~~ high-frequency limit (Figure 5, right). For the model with connected cracks, as frequency decreases, the P-wave velocity decreases, reaching its minimum at low frequencies (10^1-$10^{3.5}$ Hz).

Figures 6-7 show the quasi-shear (SV) and the pure shear (SH) phase velocities as functions of the phase angle of the numerical models with connected and disconnected cracks (Figure 1). The SV-wave velocity is strongly frequency-dependent in both the XZ- and YZ planes. The SH-wave exhibits some frequency-dependent behavior in the XZ-plane and is angle- and frequency- independent in the YZ plane. It is interesting that the SV-waves in two different planes have different velocities at 0 and 90 phase angles, which is due to their different wave polarization. The SV-wave in the YZ plane has the same polarization as the SH-wave in the XZ plane, their velocities are equivalent at the 0 and 90 phase angles. The same conclusion is valid for the SV-wave in the XZ plane and the SH-wave in the YZ plane. A slight discrepancy (around 0.5%) between the SV-wave velocities for the disconnected crack model (Figure 6, dashed red line) and the high-frequency velocity for the connected crack model (Figure 6, green line) at phase angles of 0, 90 and 180 degrees is due to the crack separation.

Due to the symmetry of the model, the behaviors of the P-, SV-, SH-wave phase velocities in the XZ- and XY-planes are ~~the same~~identical, thus the results in the XY-plane are not shown here.

4.4 Quantitative analysis of the frequency-dependent anisotropy

First, we quantify the Thomsen-type anisotropic parameters (Thomsen, 1986) for orthorhombic media (Tsvankin, 1997; Bakulin et al., 2000a). Then, we quantify the universal elastic anisotropy index (Ranganathan and Ostoja-Starzewski, 2008) and the two parameters which define the anisotropy strength in bulk and shear modes. All these anisotropy measures highlight

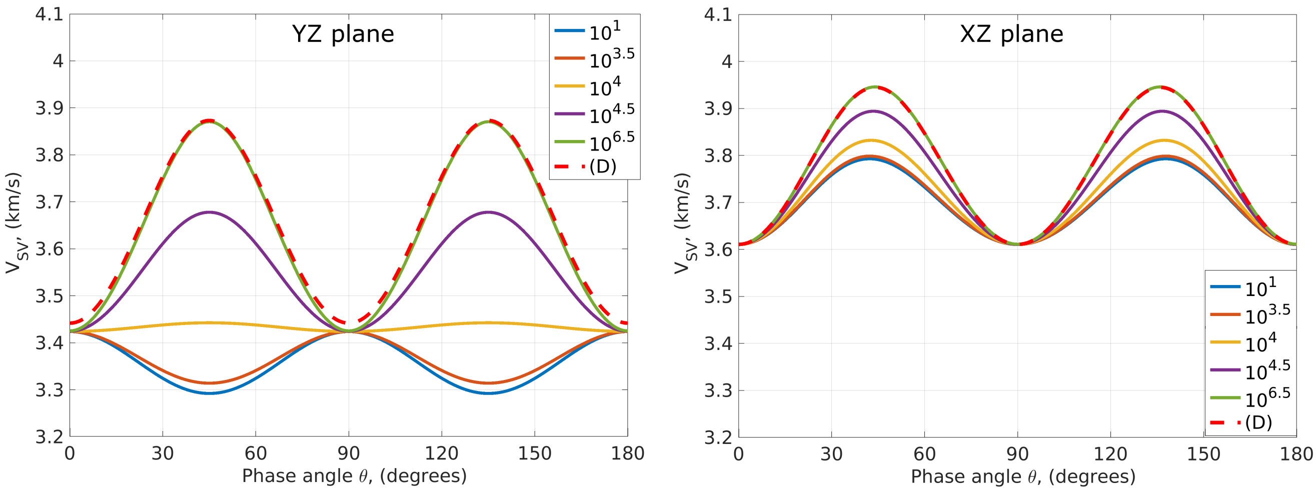

Figure 6. SV-wave phase velocity versus phase angle in the YZ-plane (left) and the XZ-plane (right). Curves 10^1-$10^{6.5}$ denote the frequency of the P-wave for the model with connected cracks. (D) — denotes the P-wave for the model with disconnected cracks.

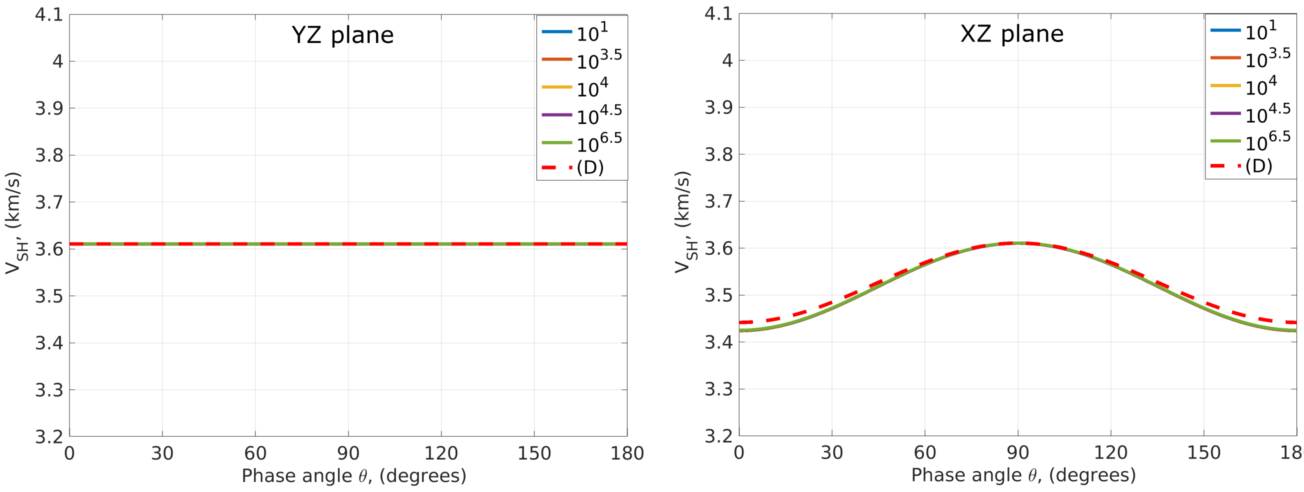

Figure 7. SH-wave phase velocity versus phase angle in the YZ-plane (left) and the XZ-plane (right). Curves 10^1-$10^{6.5}$ denote the frequency of the P-wave for the model with connected cracks. (D) — denotes the P-wave for the model with disconnected cracks.

different frequency-dependent features of the models. Our results shown in Figure 4 (frequency-dependent elastic moduli) are used as input to quantify these anisotropy measures.

4.4.1 Thomsen-type parameters

Thomsen-type anisotropic parameters (ϵ, δ, γ) describe the P-wave anisotropy — ϵ, the shape of the P-wave phase velocity at different phase angles — δ and the S-wave anisotropy — γ: each set of three parameters corresponds to one plane. Thus, for our model symmetry, there are two different planes — YZ and XZ (because the XZ plane is equivalent to the XY plane). In this study, we refer to Thomsen parameters $\mid \epsilon \mid, \mid \delta \mid, \mid \gamma \mid \in [0; 0.1]$ as to weak elastic anisotropy ($\mid \cdot \mid$ corresponds to the absolute value), $\mid \epsilon \mid, \mid \delta \mid, \mid \gamma \mid \in [0.1; 0.15]$ as to moderate elastic anisotropy and $\mid \epsilon \mid, \mid \delta \mid, \mid \gamma \mid \in [0.15; +\infty]$ as to strong elastic anisotropy. The choice of these intervals is based on the divergence between the exact and approximate (by using Thomsen parameters) equations for the P-wave phase velocities in cracked media.

Figure 8 shows the Thomsen-type anisotropy parameters in the YZ and XZ planes (formulas are given in Appendix B). In the ~~high frequency~~ high-frequency limit, all anisotropy parameters are the same for both models with connected and disconnected cracks. Furthermore, for the model with disconnected cracks, all anisotropy parameters are frequency independent because the stiffness tensor is frequency independent. For the model with connected cracks, several anisotropy parameters are frequency dependent due to squirt flow.

In the YZ plane, parameters ϵ^{YZ} and γ^{YZ} are zero for both models. The parameter δ^{YZ} is frequency dependent and controls the shape of the P- wave phase velocity between 0 and 90 degrees. In the ~~high frequency~~ high-frequency limit, δ^{YZ} exhibits the maximum negative value which correponds to strong elastic anisotropy. As frequency decreases, δ^{YZ} also decreases reaching zero value around 10^4 Hz and, then, δ^{YZ} increases reaching its positive maximum at low frequencies which corresponds to weak elastic anisotropy; the positive maximum is approximately $1/3$ of the absolute value of its negative maximum. It is interesting, that δ^{YZ} changes sign from negative to positive which is indeed observed in the P-wave velocity behavior (Figure 5, left) as P-wave velocity changes polarity with frequency. This was also observed by Barbosa et al. (2017) in the framework of Biot's theory. This polarity change has a fully mechanical nature. In the ~~high frequency~~ high-frequency limit, cracks behave as hydraulically isolated and fluid highly stiffens the normal compliance of the cracks (not tangential). As frequency decreases, fluid started to flow from more compliant to stiffer cracks as a response to the applied displacement boundary condition. $\delta^{(yz)} = 0$ corresponds to zero anisotropy; the numerator of δ^{YZ} is $[c_{23}(\omega) + c_{44}(\omega)]^2 - [c_{33}(\omega) - c_{44}(\omega)]^2$ (see Appendix B). Therefore, for zero anisotropy $c_{23}(\omega) + c_{44}(\omega)$ must be equal to $c_{33}(\omega) - c_{44}(\omega)$. The function $c_{44}(\omega)$ is constant across the whole frequency range, $c_{23}(\omega)$ is strictly decreasing with frequency and $c_{33}(\omega)$ is strictly increasing with frequency (Figure 4). At a certain frequency (here it is at $\approx 10^4$ Hz), the c_{33} and c_{23} components are in such combination that $c_{23}(10^4) + c_{44}(10^4) \approx c_{33}(10^4) - c_{44}(10^4)$, so $\delta^{YZ} = 0$ and the P-wave velocity in the YZ plane behaves as in a fully isotropic media.

In the XZ plane, ϵ^{XZ} and δ^{XZ} are frequency dependent in the model with connected cracks. ϵ^{XZ} exhibits moderate elastic anisotropy at low frequencies while δ^{XZ} exhibits moderate elastic anisotropy at high frequencies. Other parameters are frequency independent and exhibit certain non-zero value from weak to moderate elastic anisotropy.

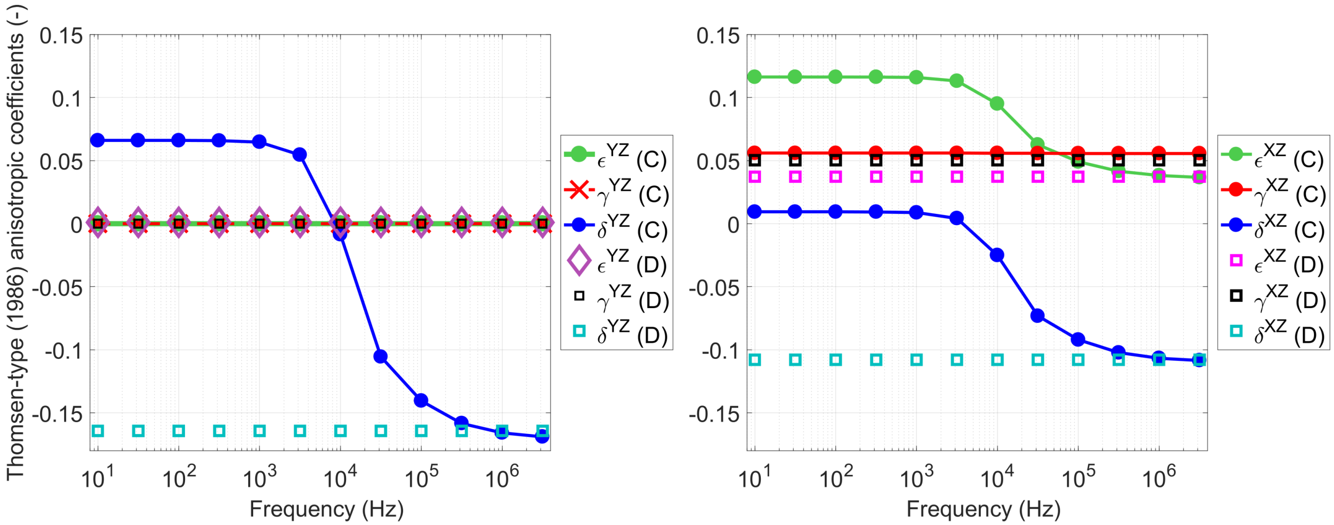

Figure 8. Thomsen-type anisotropic parameters in the YZ (left) and XZ (right) planes.

4.4.2 The universal elastic anisotropy index

The universal elastic anisotropy index A^U (Ranganathan and Ostoja-Starzewski, 2008) is widely used to measure the anisotropy strength in crystallography, engineering and material science. This parameter is designed to evaluate the anisotropy strength of crystals having any elastic symmetry class (Ranganathan and Ostoja-Starzewski, 2008). Since A^U is a scalar, it gives a simple and fast identification of the overall anisotropy strength of a model. $A^U = 0$ corresponds to zero anisotropy of a model while the discrepancy of A^U from zero defines the anisotropy strength and accounts for both the shear and the bulk contributions simultaneously. In analogy to the universal elastic anisotropy index, two other parameters are adopted which define the anisotropy strength in bulk A^{bulk} and in shear A^{shear}. As far as we are concerned, these parametrs have not been widely used in earth sciences, only a few studies were found. Almqvist and Mainprice (2017) applied the universal elastic anisotropy index and similar two parameters for bulk and shear to study seismic properties and anisotropy of the continental crust. Kube and De Jong (2016); Duffy (2018); Vieira et al. (2019) applied A^U to quantify the elastic anisotropy of polycrystals. A brief review of these anisotropic measures and all necessary equations for their calculation are provided in Appendix C.

Figure 9 shows the universal elastic anisotropy index A^U and the anisotropy measures in bulk $A^{bulk}(\omega)$ and shear A^{shear}. For the model with disconnected cracks, A^U is constant and frequency independent (Figure 9, black line). Because A^U has a certain small value (about 0.058), the model with disconnected cracks exhibit a certain small anisotropy. For the model with connected cracks, A^U in the ~~high frequency~~ high-frequency limit is almost the same as for the model with disconnected cracks (Figure 9, red line) (the nature of the discrepancy is related to the region containing the crack intersection~~and explained in the previous section~~). For the model with connected cracks, the overall anisotropy slightly decreases towards lower frequencies until $10^{4.3}$ Hz, reaching its minimum of 0.048 (Figure 9, red line). This local minimum indeed corresponds to the c_{23} attenuation

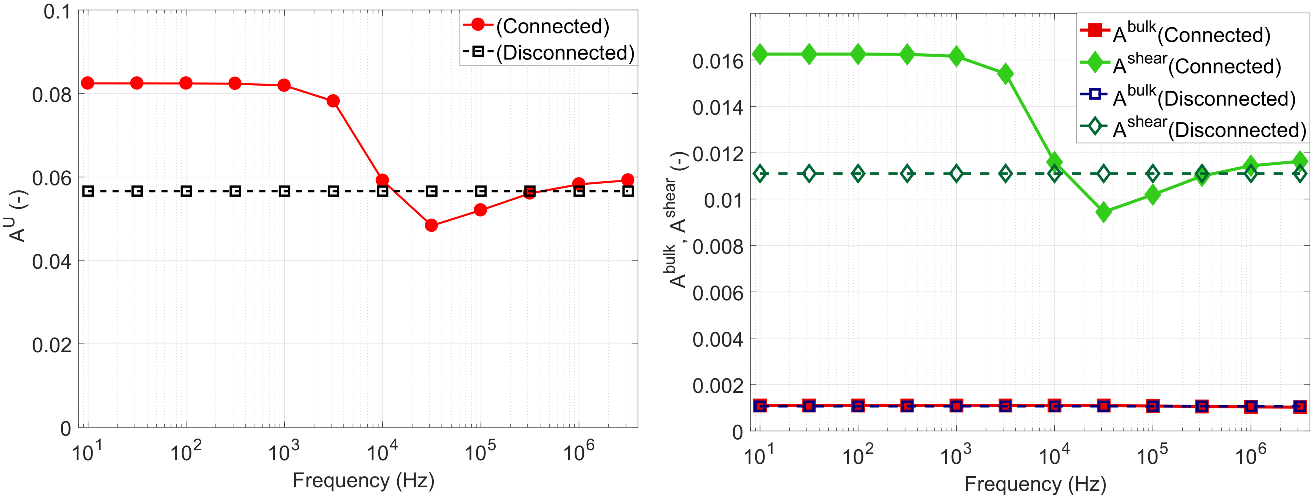

Figure 9. The universal elastic anisotropy index measure A^U versus frequency (left) and the anisotropy measures in bulk and shear (A^{bulk} and A^{shear}) (right). These plots show that the overall anisotropy if the model increases in the low frequencies due to fluid flow.

peak (Figure 4~~, (e)~~c). Then, still towards lower frequencies, $A^U(\omega)$ increases reaching its maximum of 0.083 at frequencies below 10^3 Hz (Figure 9, red line). Thus, the overall anisotropy of the model mainly increases due to squirt flow between the cracks, so the cracks connectivity increases the overall anisotropy of the model towards low frequencies.

The anisotropy measure in bulk A^{bulk} is constant and frequency independent for the models with connected and disconnected cracks (Figure 9 , right). It means that fluid flow do not affect bulk properties of the model neither the anisotropy strength in bulk. On the other hand, the anisotropy measure in shear $A^{shear}(\omega)$ basically reproduces the behavior of the universal elastic anisotropy index measure A^U. Therefore, one can conclude that the fluid flow changes anisotropy in shear mode, but not in bulk mode.

5 Discussion

5.1 Elastic anisotropy

Thomsen-type anisotropic parameters provide a very detailed description of the velocity anisotropy in different planes. Most importantly, only a limited number of the stiffness tensor coefficients is needed to calculate ϵ, δ, γ in each plane. Thus, Thomsen parameters can be used to quantify the medium anisotropy using seismic data. On the other hand, when all components of the stiffness tensor are known and the model's symmetry is low, it is difficult to analyse the overall anisotropy due to a large number of Thomsen parameters. For example, if the model exhibits orthorhombic symmetry, one should analyze nine Thomsen anisotropic parameters (three in each plane). Due to a large number of Thomsen parameters in this study, it is difficult to evaluate whether the overall medium's anisotropy is increasing or decreasing with frequency and how far the current model is from the closest isotropy. Thus, in addition to (or instead of) the Thomsen-type anisotropic parameters, the universal elastic anisotropy index can be used. The universal elastic anisotropy index A^U and the related measures in bulk A^{bulk} and shear A^{shear} provide the overall description of the anisotropy strength regardless of the model's complexity. The calculation of these parameters is as simple as the calculation of the Thomsen parameters. An obvious disadvantage of the universal elastic anisotropy index (and related measures) is that it requires knowledge of the full stiffness tensor. Thus, this anisotropic measure can be useful to evaluate results of numerical simulations, of laboratory experiments and for measuring the anisotropy of single crystals.

The analysis of two sets of anisotropic measures shows that (i) the the overall anisotropy of the model with connected cracks (Figure 1) mainly increases due to squirt flow towards low frequencies with a slight local decrease at intermediate frequencies (Figure 9 (left)), (ii) in the YZ plane, the magnitude of the "delta" anisotropy parameter decreases, reaches zero and then increases again (reaching $\approx 1/3$ of its ~~high frequency~~ high-frequency value) towards low frequencies (Figure 8 (left), blue curve) and (iii) in the XZ plane, the "delta" anisotropy parameter decreases towards low frequencies (Figure 8 (right), blue curve) while the "epsilon" anisotropy parameter increases (Figure 8 (right), green curve).

5.2 Comparison against previous works

In this study, we numerically solve a coupled fluid-solid deformation problem at the pore scale. If we consider the mesoscopic scale scenario and use Biot's (1941) equations, the fluid flow effects on the effective moduli are equivavalent to that of the coupled elastic-Stokes equations (as in the present study), as it was shown by Quintal et al. (2016). The frequency-dependent anisotropy due to fluid flow at the mesoscopic scale for orthogonal fracture sets with different degrees of connectivity was numerically studied by Rubino et al. (2017) but their study was limitted to two dimensions. The main conclusion of Rubino et al. (2017) is that the anisotropy decreases with fracture connectivity in the seismic frequency band due to fluid flow between connected fractures. The YZ-plane in the present 3D numerical model is resonably equivalent to the 2D numerical model of Rubino et al. (2017) as well as the physical mechanism under consideration. The results of Rubino et al. (2017) are reflected in Figure 5 of this study. However, a more in depth analysis shows that the anisotropy in the YZ-plane decreases, reaches zero and then increases again towards low frequencies due to squirt flow (Figure 5 (left), green, yellow and blue curves, respectively). Moreover, our present study shows that the overall anisotropy of the model with cracks of finite length actually increases due to fluid flow between interconnected cracks (Figures 8, 9). This conclusion is not universal and is valid only for a specific set of model parameters.

Barbosa et al. (2017) performed a more detailed study of seismic anisotropy for a similar fracture geometry in two dimensions, as in the study of Rubino et al. (2017), specifying that the decrease in anosotropy is described by the anisotropy parameter δ while ϵ is zero. Furthermore, they observed a polarity change of the P-wave phase velocity behavior with frequency. In the present study, the "delta" anisotropy parameter in the YZ-plane is more pronounced in the ~~low frequency~~ low-frequency limit (Figure 5 (left), blue curve) compared to the work of Barbosa et al. (2017) due to different material properties and the three-dimensional nature of the present model configuration.

In summary, fluid flow effects on seismic anisotropy are non-linear with a possible increase and decrease in the elastic anisotropy at different frequencies. These two extreme cases, the maximum negative and the maximum positive δ parameter (and, hence, P-wave velocity) in the YZ plane, correspond to the relaxed and unrelaxed states. In other words, seismic anisotropy may behave completely different in different scenarios, therefore, more studies should be performed, especially with the sensitivity analysis of model parameters.

5.3 A qualitative comparison against analytical models

Numerical simulations are useful but analytical models are especially attractive since they help us to better understand the physics and do not require sophisticated numerical simulations. The limitations of the analytical solutions are restricted to simple pore space geometry and some assumptions related to physics are needed to derive the closed form analytical formulas. Such a comparison of the numerical results against an analytical solution has been performed by Alkhimenkov et al. (2020) for a different pore space geometry. Unfortunately, there is no analytical solution for the present study considering a periodic distribution of intersecting cracks in three-dimensions. But the qualitative comparison of the low- and high-frequency limits (which correspond to relaxed and unrelaxed states) is possible (Mavko and Jizba, 1991). Several analytical studies show that that the anisotropy (described by Thompson's parameters) is, in general, more pronounced at high frequencies than at low frequencies (Guéguen and Sarout, 2009, 2011). In the relaxed state, one can calculate the effective dry elastic moduli and use Gassmann's equations to obtain the effective moduli of the saturated medium. In the unrelaxed state, one can calculate the effective elastic moduli by restricting fluid flow (by using zero displacement boundary conditions in the cracks intersections). ~~In other words, seismic anisotropy may behave completely different in different scenarios, therefore, more studies should be performed, especially with the sensitivity analysis of model parameters~~The low- and high-frequency limits for elastic moduli have been calculated using these semi-analytical approaches and numerical results have been reproduced.

6 Conclusions

We have numerically calculated the frequency-dependent elastic moduli of a fluid-saturated porous medium caused by squirt flow. The considered 3D numerical models consist of two perpendicular connected or disconnected cracks embedded in a solid grain material. Cracks are represented by very flat cylinders filled with a fluid. Grains are described as a linear isotropic elastic material while the fluid phase is described by the quasistatic linearized compressible Navier-Stokes momentum equation.

We showed that seismic velocities are azimuth-, angle- and frequency-dependent due to squirt flow between connected cracks. The resulting elastic frequency-dependent anisotropy was analylized by using the Thomsen-type anisotropic parameters and the universal elastic anisotropy index. The latter is a scalar parameter which can be used to analyse the overall anisotropy of the model and its divergence from the closest isotropy. We showed that the seismic anisotropy may locally decrease as well as increase due to squirt flow in one specific plane. However, the overall anisotropy of the model mainly increases due to squirt flow between the cracks towards low frequencies. In the model with disconnected cracks, no fluid flow occurs and, thus, the effective properties of the model correspond to the elastic limit. The elastic limit is equivalent to the high-frequency limit for the model with connected cracks. Seismic velocities are only azimuth- and angle- dependent as for a fully elastic material and they are independent of frequency. ~~The elastic limit is equivalent to the high frequency limit for the model with connected cracks.~~

~~Our conclusion is that squirt flow do affect effective elastic~~ In summary, squirt flow does affect effective mechanical properties of cracked rocks and, thus, seismic velocity anisotropy. Given that seismic anisotropy variations with frequency are very sensitive to the pore space geometry and material properties, ~~we cannot make a very~~ it is difficult to make a general prediction. According to our study, the effective frequency-dependent response of a cracked medium is different in different planes. The local response (in a certain plane) is controlled by cracks orientation, which is the key parameter. The magnitude of the frequency-dependent response (i.e. the dispersion and attenuation) is controlled by crack compliances, crack porosity and their fluid content (dry or liquid-saturation will cause completely different behavior). Most importantly, crack porosity is a very important parameter in fluid-saturated rocks (contrary to dry rocks) since it defines the volume of fluid content which may flow due to wave propagation, causing wave attenuation and dispersion.

Appendix A: Boundary conditions for c_{ij} off-diagonal components

Let's consider a cuboid, volume $V = (0, Lx) \times (0, Ly) \times (0, Lz)$ and Γ its boundary $\Gamma = \Gamma^{xz0} \cup \Gamma^{xzL} \cup \Gamma^{yz0} \cup \Gamma^{yzL} \cup \Gamma^{xy0} \cup \Gamma^{xyL}$, where, for example, Γ^{xz0} represents a xz plane with zero coordinate and Γ^{xzL} represents a xz plane with Ly coordinate etc. There are six planes in total.

The mixed test for the c_{13} component can be derived from the anisotropic stress-strain relation (Hooke's law) (similarly to the c_{13} component in a VTI medium ~~(?)).~~ (Alkhimenkov et al., 2020)),

Γ^{xyL} is set to $u_{zz} = \Delta u$; u_{xx}, u_{yy} are free
Γ^{yzL} is set to $u_{xx} = \Delta u$; u_{zz}, u_{yy} are free,

where $\Delta u = 10^{-6}$. In other four planes, the normal component of the displacement is set to zero, other components are free. The the stress-strain relation for the $\langle\sigma_1\rangle$ stress component is

$$\langle\sigma_1\rangle = c_{11}\langle\epsilon_1\rangle + c_{12}\langle\epsilon_2\rangle + c_{13}\langle\epsilon_3\rangle. \tag{A1}$$

Using the described above boundary conditions and setting $\langle\epsilon_2\rangle = 0$, equation (A1) becomes

$$\langle\sigma_1\rangle = c_{11}\langle\epsilon_1\rangle + c_{13}\langle\epsilon_3\rangle. \tag{A2}$$

Equation (A2) can be solved for the c_{13} component, the solution is

$$c_{13} = \frac{\langle\sigma_1\rangle}{\langle\epsilon_1\rangle} - c_{11}. \tag{A3}$$

Equation (A3) is used to calculate the c_{13} component (c_{11} is taken from the direct tests).

The mixed test for the c_{23} (in this numerical model, the c_{23} is dispersive) component again can be derived from the anisotropic stress-strain relation (Hooke's law) (similarly to the previous test).

Γ^{xyL} is set to $u_{zz} = \Delta u$; u_{xx}, u_{yy} are free
Γ^{xzL} is set to $u_{yy} = \Delta u$; u_{zz}, u_{xx} are free

In other four planes, the normal component of the displacement is set to zero, other components are free. Then, using the following equation

$$c_{23} = \frac{\langle \sigma_2 \rangle}{\langle \epsilon_2 \rangle} - c_{22}, \tag{A4}$$

the c_{23} component is calculated (c_{22} is taken from the direct test). Equations (A3)-(A4) are found from the Hooke's Law considering non-zero strains in x- and z (in y- and z) directions and, then, solving a system of two equations analytically.

Appendix B: Thomsen-type anisotropic parameters

Thomsen-type anisotropic parameters (Thomsen, 1986) are widely used in the applied geophysics community. Thomsen weak anisotropy parameters were originaly developed for vertical transverse isotropic media (Thomsen, 1986). A natural extension of these parameters to orthorhombic media was suggested by Tsvankin (1997); Bakulin et al. (2000a). These parameters correspond to the anisotropy of the compression and shear waves in orthorhombic media in different Cartesian propagation planes. In the YZ-plane, Thomsen-type anisotropic parameters are

$$\epsilon^{(YZ)}(\omega) = \frac{c_{22}(\omega) - c_{33}(\omega)}{2c_{33}(\omega)}, \;\; \gamma^{(YZ)}(\omega) = \frac{c_{66}(\omega) - c_{55}(\omega)}{2c_{55}(\omega)}, \tag{B1}$$

and

$$\delta^{(YZ)}(\omega) = \frac{\left[c_{23}(\omega) + c_{44}(\omega)\right]^2 - \left[c_{33}(\omega) - c_{44}(\omega)\right]^2}{2c_{33}(\omega)\left[c_{33}(\omega) - c_{44}(\omega)\right]} \tag{B2}$$

In the XZ-plane, Thomsen-type anisotropic parameters are

$$\epsilon^{(XZ)}(\omega) = \frac{c_{11}(\omega) - c_{33}(\omega)}{2c_{33}(\omega)}, \;\; \gamma^{(XZ)}(\omega) = \frac{c_{66}(\omega) - c_{44}(\omega)}{2c_{44}(\omega)}, \tag{B3}$$

and

$$\delta^{(XZ)}(\omega) = \frac{\left[c_{13}(\omega) + c_{55}(\omega)\right]^2 - \left[c_{33}(\omega) - c_{55}(\omega)\right]^2}{2c_{33}(\omega)\left[c_{33}(\omega) - c_{55}(\omega)\right]}, \tag{B4}$$

Appendix C: The universal elastic anisotropy index parameter

Assuming that one deals with an anisotropic frequency-dependent effective 4-th rank stiffness tensor $\mathbf{C}$ (might be frequency dependent $\mathbf{C} \Rightarrow \mathbf{C}(\omega)$), a compliance tensor is defined as $\mathbf{S}(\omega) = \mathbf{C}(\omega)^{-1}$. Then, for each frequency, the effective single orientation 4-th rank stiffness and compliance tensors are uniformly distributed and the isotropic stiffness and compliance tensors are calculated. Averaging the single orientation stiffness tensor belongs to the Voigt assumption which is the theoretical maximum value of the isotropic elastic moduli. On the other hand, averaging the single orientation compliance tensor belongs to the Reuss assumption which is the theoretical minimum value of the isotropic elastic moduli. The resulting isotropic tensors can be expressed in terms of the spherical and deviatoric parts corresponding to bulk K and shear moduli μ:

$$\mathbf{C}^V(\omega) = 3K^V\mathbf{J} + 2\mu^V\mathbf{D} \tag{C1}$$

and

$$\mathbf{S}^R(\omega) = \frac{1}{3K^R}\mathbf{J} + \frac{1}{2\mu^R}\mathbf{D}, \tag{C2}$$

where the superscripts "^{V}" and "^{R}" correspond to Voigt and Reuss estimates, respectively. $\mathbf{J}$ and $\mathbf{D}$ are the spherical (volumetric) and deviatoric parts of the symmetric unit 4-th order tensor.

The double contraction the scalar product (quadruple contraction) of Equation (C1) and Equation (C2) gives

$$\mathbf{C}^V(\omega) :: \mathbf{S}^R(\omega) = \frac{K^V(\omega)}{K^R(\omega)} + 5\frac{\mu^V(\omega)}{\mu^R(\omega)}, \tag{C3}$$

If the effective stiffness tensor is isotropic, then $\mathbf{C}^V(\omega) = \left(\mathbf{S}^R(\omega)\right)^{-1}$ and $K^V/K^R = \mu^V/\mu^R = 1$. Therefore, when the effective stiffness tensor is isotropic, the value of Equation (C3) equals to 6 and this value increases when the effective stiffness tensor becomes anisotropic. Thus, the universal elastic anisotropy index measure A^U is defined as (Ranganathan and Ostoja-Starzewski, 2008):

$$A^U(\omega) = \frac{K^V(\omega)}{K^R(\omega)} + 5\frac{\mu^V(\omega)}{\mu^R(\omega)} - 6 \geq 0, \tag{C4}$$

In geophysics, the separation of the elastic anisotropy measure in bulk and shear modes is necessary because rocks might exhibit different frequency-dependence due to bulk and shear deformations. Therefore, in analogy to the universal elastic anisotropy index measure A^U, the anisotropy measures in bulk $A^{bulk}(\omega)$ and shear $A^{shear}(\omega)$ can be defined

$$A^{bulk}(\omega) = \frac{K^V(\omega)}{K^R(\omega)} - 1 \tag{C5}$$

and

$$A^{shear}(\omega) = \frac{G^V(\omega)}{G^R(\omega)} - 1 \tag{C6}$$

These two parameters $A^{bulk}(\omega)$ and $A^{shear}(\omega)$ obey the same interpretation as the universal elastic anisotropy index measure: $A^{bulk} = 0$ ($A^{shear} = 0$) corresponds to zero bulk (shear) anisotropy of the model while the discrepancy of A^U from zero anisotropy defines the anisotropy strength in bulk (shear).

The Voigt and Reuss estimates (K^V, K^R, μ^V and μ^R) can be calculated via simple algebraic formulas for different symmetry classes which can be found elsewhere, e.g in Ravindran et al. (1998) for orthorhombic symmetry, in Feng et al. (2012) for tetragonal symmetry and in Duffy (2018) for cubic symmetry. Thus, for orthorhombic symmetry (lowest possible symmetry created by two perpendicular sets of cracks embedded into an isotropic material), the Voigt and Reuss bulk moduli for are (written for the components of stiffness (compliance) matrices $c_{ij}(s_{ij})$, in Voigt notation)

$$K^V = \frac{1}{9}\left[(c_{11} + c_{22} + c_{33}) + 2(c_{12} + c_{13} + c_{23})\right] \tag{C7}$$

and

$$K^R = \left[(s_{11} + s_{22} + s_{33}) + 2(s_{12} + s_{13} + s_{23})\right]^{-1}. \tag{C8}$$

Similarly, the Voigt and Reuss shear moduli are (in Voigt notation)

$$\mu^V = \frac{1}{15}\left[(c_{11} + c_{22} + c_{33} - c_{12} - c_{13} - c_{23}) + 3(c_{44} + c_{55} + c_{66})\right] \tag{C9}$$

and

$$\mu^R = 15\left[4(s_{11} + s_{22} + s_{33} - s_{12} - s_{13} - s_{23}) + 3(s_{44} + s_{55} + s_{66})\right]^{-1}. \tag{C10}$$

Equations (C7)-(C10) are valid for orthorhombic symmetry and for higher symmetries: tetragonal, transverse isotropy and cubic. Thus, for evaluating the universal elastic anisotropy index A^U and the anisotropy measures in bulk $A^{bulk}(\omega)$ and shear $A^{shear}(\omega)$, one can use equations (C7)-(C10) to calculate the Voigt and Reuss estimates (K^V, K^R, μ^V and μ^R) and, then, calculate A^U using equation (C4) and $A^{bulk}(\omega)$ and $A^{shear}(\omega)$ using equations (C5) and (C6), respectively.

Author contributions. YA performed the numerical simulations and wrote the manuscript. The idea of this project was first inspired by the paper of Rubino et al. (2017). A detailed project was planed by YA and BQ. EC, SL and BQ provided many ideas and suggestions which influenced the project path and helped writing the manuscript.

Competing interests. The authors declare that they have no conflict of interest.

Acknowledgements. This research is funded by the Swiss National Science Foundation, project number 172691. Yury Alkhimenkov thanks J. Germán Rubino (CONICET, Centro Atómico Bariloche, Argentina) for fruitful discussions on the frequency-dependent anisotropy due to fluid flow~~. We thank~~, Nicolás D. Barbosa (University of Geneva, Switzerland) for fruitful discussions regarding the polarity change of the P-wave velocity with frequency~~. We thank~~, and Irina Bayuk (Russian Academy of Sciences, Russia) for ~~useful~~ enlightening discussions regarding the fourth-rank tensors averaging and the elastic symmetry classes.

References

Adelinet, M., Fortin, J., Guéguen, Y., Schubnel, A., and Geoffroy, L.: Frequency and fluid effects on elastic properties of basalt: Experimental investigations, Geophysical Research Letters, 37, 2010.

Alkhimenkov, Y., Caspari, E., Gurevich, B., Barbosa, N. D., Glubokovskikh, S., Hunziker, J., and Quintal, B.: Frequency-dependent attenuation and dispersion caused by squirt flow: Three-dimensional numerical study, Geophysics, 85, 1–71, 2020.

Almqvist, B. S. and Mainprice, D.: Seismic properties and anisotropy of the continental crust: predictions based on mineral texture and rock microstructure, Reviews of Geophysics, 55, 367–433, 2017.

Amalokwu, K., Best, A. I., and Chapman, M.: Effects of aligned fractures on the response of velocity and attenuation ratios to water saturation variation: a laboratory study using synthetic sandstones, Geophysical Prospecting, 64, 942–957, 2016.

Andrä, H., Combaret, N., Dvorkin, J., Glatt, E., Han, J., Kabel, M., Keehm, Y., Krzikalla, F., Lee, M., Madonna, C., et al.: Digital rock physics benchmarks—Part I: Imaging and segmentation, Computers & Geosciences, 50, 25–32, 2013a.

Andrä, H., Combaret, N., Dvorkin, J., Glatt, E., Han, J., Kabel, M., Keehm, Y., Krzikalla, F., Lee, M., Madonna, C., et al.: Digital rock physics benchmarks—Part II: Computing effective properties, Computers & Geosciences, 50, 33–43, 2013b.

Bakulin, A., Grechka, V., and Tsvankin, I.: Estimation of fracture parameters from reflection seismic data—Part II: Fractured models with orthorhombic symmetry, Geophysics, 65, 1803–1817, 2000a.

Bakulin, A., Grechka, V., and Tsvankin, I.: Estimation of fracture parameters from reflection seismic data—Part II: Fractured models with orthorhombic symmetry, Geophysics, 65, 1803–1817, 2000b.

Barbosa, N. D., Rubino, J. G., Caspari, E., and Holliger, K.: Sensitivity of seismic attenuation and phase velocity to intrinsic background anisotropy in fractured porous rocks: A numerical study, Journal of Geophysical Research: Solid Earth, 122, 8181–8199, 2017.

Best, A. I., Sothcott, J., and McCann, C.: A laboratory study of seismic velocity and attenuation anisotropy in near-surface sedimentary rocks, Geophysical Prospecting, 55, 609–625, 2007.

Biot, M. A.: Generalized theory of acoustic propagation in porous dissipative media, The Journal of the Acoustical Society of America, 34, 1254–1264, 1962.

Brajanovski, M., Gurevich, B., and Schoenberg, M.: A model for P-wave attenuation and dispersion in a porous medium permeated by aligned fractures, Geophysical Journal International, 163, 372–384, 2005.

Carcione, J. M., Gurevich, B., Santos, J. E., and Picotti, S.: Angular and frequency-dependent wave velocity and attenuation in fractured porous media, Pure and Applied Geophysics, 170, 1673–1683, 2013.

Caspari, E., Novikov, M., Lisitsa, V., Barbosa, N. D., Quintal, B., Rubino, J. G., and Holliger, K.: Attenuation mechanisms in fractured fluid-saturated porous rocks: a numerical modelling study, Geophysical Prospecting, 67, 935–955, 2019.

Chapman, M.: Frequency-dependent anisotropy due to meso-scale fractures in the presence of equant porosity, Geophysical Prospecting, 51, 369–379, 2003.

Chapman, M., Zatsepin, S. V., and Crampin, S.: Derivation of a microstructural poroelastic model, Geophysical Journal International, 151, 427–451, 2002.

Chapman, S., Borgomano, J. V., Yin, H., Fortin, J., and Quintal, B.: Forced oscillation measurements of seismic wave attenuation and stiffness moduli dispersion in glycerine-saturated Berea sandstone, Geophysical Prospecting, 67, 956–968, 2019.

Das, V., Mukerji, T., and Mavko, G.: Numerical simulation of coupled fluid-solid interaction at the pore scale: A digital rock-physics technology, Geophysics, 84, WA71–WA81, 2019.

Duffy, T. S.: Single-crystal elastic properties of minerals and related materials with cubic symmetry, American Mineralogist: Journal of Earth and Planetary Materials, 103, 977–988, 2018.

Dvorkin, J., Mavko, G., and Nur, A.: Squirt flow in fully saturated rocks, Geophysics, 60, 97–107, 1995.

Fedorov, F. I.: Theory of elastic waves in crystals, 1968.

Feng, J., Xiao, B., Zhou, R., Pan, W., and Clarke, D. R.: Anisotropic elastic and thermal properties of the double perovskite slab–rock salt layer Ln2SrAl2O7 (Ln= La, Nd, Sm, Eu, Gd or Dy) natural superlattice structure, Acta Materialia, 60, 3380–3392, 2012.

Grab, M., Quintal, B., Caspari, E., Maurer, H., and Greenhalgh, S.: Numerical modeling of fluid effects on seismic properties of fractured magmatic geothermal reservoirs, Solid Earth, 8, 255–279, 2017.

Grechka, V. and Kachanov, M.: Effective elasticity of rocks with closely spaced and intersecting cracks, Geophysics, 71, D85–D91, 2006.

Guéguen, Y. and Sarout, J.: Crack-induced anisotropy in crustal rocks: predicted dry and fluid-saturated Thomsen's parameters, Physics of the Earth and Planetary Interiors, 172, 116–124, 2009.

Guéguen, Y. and Sarout, J.: Characteristics of anisotropy and dispersion in cracked medium, Tectonophysics, 503, 165–172, 2011.

Guo, J., Germán Rubino, J., Barbosa, N. D., Glubokovskikh, S., and Gurevich, B.: Seismic dispersion and attenuation in saturated porous rocks with aligned fractures of finite thickness: Theory and numerical simulations—Part 2: Frequency-dependent anisotropy, Geophysics, 83, WA63–WA71, 2017a.

Guo, J., Rubino, J. G., Glubokovskikh, S., and Gurevich, B.: Effects of fracture intersections on seismic dispersion: theoretical predictions versus numerical simulations, Geophysical Prospecting, 65, 1264–1276, 2017b.

Guo, J., Rubino, J. G., Glubokovskikh, S., and Gurevich, B.: Dynamic seismic signatures of saturated porous rocks containing two orthogonal sets of fractures: theory versus numerical simulations, Geophysical Journal International, 213, 1244–1262, 2018.

Gurevich, B., Makarynska, D., de Paula, O. B., and Pervukhina, M.: A simple model for squirt-flow dispersion and attenuation in fluid-saturated granular rocks, Geophysics, 75, N109–N120, 2010.

Hunziker, J., Favino, M., Caspari, E., Quintal, B., Rubino, J. G., Krause, R., and Holliger, K.: Seismic attenuation and stiffness modulus dispersion in porous rocks containing stochastic fracture networks, Journal of Geophysical Research: Solid Earth, 123, 125–143, 2018.

Kachanov, M. and Sevostianov, I.: Micromechanics of materials, with applications, vol. 249, Springer, 2018.

Kube, C. M. and De Jong, M.: Elastic constants of polycrystals with generally anisotropic crystals, Journal of Applied Physics, 120, 165 105, 2016.

Landau, L. and Lifshitz, E.: Course of theoretical physics. vol. 6: Fluid mechanics, London, 1959a.

Landau, L. D. and Lifshitz, E. M.: Course of Theoretical Physics Vol 7: Theory and Elasticity, Pergamon press, 1959b.

Lissa, S., Barbosa, N. D., Rubino, J., and Quintal, B.: Seismic attenuation and dispersion in poroelastic media with fractures of variable aperture distributions, Solid Earth, 10, 1321–1336, 2019.

Markov, A., Abaimov, S., Sevostianov, I., Kachanov, M., Kanaun, S., and Akhatov, I.: The effect of multiple contacts between crack faces on crack contribution to the effective elastic properties, International Journal of Solids and Structures, 163, 75–86, 2019.

Masson, Y. J. and Pride, S.: On the correlation between material structure and seismic attenuation anisotropy in porous media, Journal of Geophysical Research: Solid Earth, 119, 2848–2870, 2014.

Maultzsch, S., Chapman, M., Liu, E., and Li, X. Y.: Modelling frequency-dependent seismic anisotropy in fluid-saturated rock with aligned fractures: implication of fracture size estimation from anisotropic measurements, Geophysical Prospecting, 51, 381–392, 2003.

Mavko, G. and Jizba, D.: Estimating grain-scale fluid effects on velocity dispersion in rocks, Geophysics, 56, 1940–1949, 1991.

Mavko, G. and Nur, A.: Melt squirt in the asthenosphere, Journal of Geophysical Research, 80, 1444–1448, 1975.

Mavko, G., Mukerji, T., and Dvorkin, J.: The rock physics handbook: Tools for seismic analysis of porous media, Cambridge university press, 2009.

Mayr, S. I. and Burkhardt, H.: Ultrasonic properties of sedimentary rocks: effect of pressure, saturation, frequency and microcracks, Geophysical Journal International, 164, 246–258, 2006.

Mikhaltsevitch, V., Lebedev, M., and Gurevich, B.: A laboratory study of attenuation and dispersion effects in glycerol-saturated Berea sandstone at seismic frequencies, in: SEG Technical Program Expanded Abstracts 2015, pp. 3085–3089, Society of Exploration Geophysicists, 2015.

Müller, T. M., Gurevich, B., and Lebedev, M.: Seismic wave attenuation and dispersion resulting from wave-induced flow in porous rocks—A review, Geophysics, 75, 75A147–75A164, 2010.

Nemat-Nasser, S. and Hori, M.: Micromechanics: overall properties of heterogeneous materials, vol. 37, Elsevier, 2013.

O'connell, R. and Budiansky, B.: Measures of dissipation in viscoelastic media, Geophysical Research Letters, 5, 5–8, 1978.

O'Connell, R. J. and Budiansky, B.: Viscoelastic properties of fluid-saturated cracked solids, Journal of Geophysical Research, 82, 5719–5735, 1977.

Pimienta, L., Fortin, J., and Guéguen, Y.: Experimental study of Young's modulus dispersion and attenuation in fully saturated sandstones, Geophysics, 80, L57–L72, 2015.

Pride, S. R., Berryman, J. G., and Harris, J. M.: Seismic attenuation due to wave-induced flow, Journal of Geophysical Research: Solid Earth, 109, 2004.

Quintal, B., Jänicke, R., Rubino, J. G., Steeb, H., and Holliger, K.: Sensitivity of S-wave attenuation to the connectivity of fractures in fluid-saturated rocks, Geophysics, 79, WB15–WB24, 2014.

Quintal, B., Rubino, J. G., Caspari, E., and Holliger, K.: A simple hydromechanical approach for simulating squirt-type flow, Geophysics, 81, D335–D344, 2016.

Quintal, B., Caspari, E., Holliger, K., and Steeb, H.: Numerically quantifying energy loss caused by squirt flow, Geophysical Prospecting, 67, 2196–2212, 2019.

Ranganathan, S. I. and Ostoja-Starzewski, M.: Universal elastic anisotropy index, Physical Review Letters, 101, 055 504, 2008.

Ravindran, P., Fast, L., Korzhavyi, P. A., Johansson, B., Wills, J., and Eriksson, O.: Density functional theory for calculation of elastic properties of orthorhombic crystals: Application to TiSi 2, Journal of Applied Physics, 84, 4891–4904, 1998.

Rubino, J., Caspari, E., Müller, T. M., and Holliger, K.: Fracture connectivity can reduce the velocity anisotropy of seismic waves, Geophysical Journal International, 210, 223–227, 2017.

Rubino, J Germán, J., Guarracino, L., Müller, T. M., and Holliger, K.: Do seismic waves sense fracture connectivity?, Geophysical Research Letters, 40, 692–696, 2013.

Saxena, N. and Mavko, G.: Estimating elastic moduli of rocks from thin sections: Digital rock study of 3D properties from 2D images, Computers & geosciences, 88, 9–21, 2016.

Sayers, C. and Kachanov, M.: Microcrack-induced elastic wave anisotropy of brittle rocks, Journal of Geophysical Research: Solid Earth, 100, 4149–4156, 1995.

Sayers, C. M.: Stress-dependent elastic anisotropy of sandstones, Geophysical prospecting, 50, 85–95, 2002.

Schenk, O. and Gärtner, K.: Solving unsymmetric sparse systems of linear equations with PARDISO, Future Generation Computer Systems, 20, 475–487, 2004.

Schoenberg, M. and Sayers, C. M.: Seismic anisotropy of fractured rock, Geophysics, 60, 204–211, 1995.

Subramaniyan, S., Quintal, B., Madonna, C., and Saenger, E. H.: Laboratory-based seismic attenuation in Fontainebleau sandstone: Evidence of squirt flow, Journal of Geophysical Research: Solid Earth, 120, 7526–7535, 2015.

Thomsen, L.: Weak elastic anisotropy, Geophysics, 51, 1954–1966, 1986.

Tillotson, P., Sothcott, J., Best, A. I., Chapman, M., and Li, X.-Y.: Experimental verification of the fracture density and shear-wave splitting relationship using synthetic silica cemented sandstones with a controlled fracture geometry, Geophysical Prospecting, 60, 516–525, 2012.

Tillotson, P., Chapman, M., Sothcott, J., Best, A. I., and Li, X.-Y.: Pore fluid viscosity effects on P-and S-wave anisotropy in synthetic silica-cemented sandstone with aligned fractures, Geophysical Prospecting, 62, 1238–1252, 2014.

Trofimov, A., Drach, B., Kachanov, M., and Sevostianov, I.: Effect of a partial contact between the crack faces on its contribution to overall material compliance and resistivity, International Journal of Solids and Structures, 108, 289–297, 2017.

Tsvankin, I.: Anisotropic parameters and P-wave velocity for orthorhombic media, Geophysics, 62, 1292–1309, 1997.

Tsvankin, I.: Seismic signatures and analysis of reflection data in anisotropic media, Society of Exploration Geophysicists, 2012.

Tsvankin, I. and Grechka, V.: Seismology of azimuthally anisotropic media and seismic fracture characterization, Society of Exploration Geophysicists, 2011.

Vieira, R. T., de Bortoli, D., de Carvalho, M. V., and Pires, F. A.: The role of elastic anisotropy on the macroscopic constitutive response and yield onset of cubic oligo-and polycrystals, International Journal of Plasticity, 2019.

Zhang, Y. and Toksöz, M. N.: Computation of dynamic seismic responses to viscous fluid of digitized three-dimensional Berea sandstones with a coupled finite-difference method, The Journal of the Acoustical Society of America, 132, 630–640, 2012.

Zhang, Y., Song, L., Deffenbaugh, M., and Toksöz, M. N.: A finite difference method for a coupled model of wave propagation in poroelastic materials, The Journal of the Acoustical Society of America, 127, 2847–2855, 2010.